



HAL
open science

Effect of drying temperature on the properties of alkali-activated binders - Recommendations for sample preconditioning

Vincent Trincal, Virginie Benavent, Hugo Lahalle, Bastien Balsamo, Gabriel Samson, Cédric Patapy, Yoann Jainin, Martin Cyr

► To cite this version:

Vincent Trincal, Virginie Benavent, Hugo Lahalle, Bastien Balsamo, Gabriel Samson, et al.. Effect of drying temperature on the properties of alkali-activated binders - Recommendations for sample preconditioning. Cement and Concrete Research, 2022, 151, pp.106617. 10.1016/j.cemconres.2021.106617 . hal-03414263

HAL Id: hal-03414263

<https://hal.insa-toulouse.fr/hal-03414263>

Submitted on 16 Oct 2023

HAL is a multi-disciplinary open access archive for the deposit and dissemination of scientific research documents, whether they are published or not. The documents may come from teaching and research institutions in France or abroad, or from public or private research centers.

L'archive ouverte pluridisciplinaire **HAL**, est destinée au dépôt et à la diffusion de documents scientifiques de niveau recherche, publiés ou non, émanant des établissements d'enseignement et de recherche français ou étrangers, des laboratoires publics ou privés.



Distributed under a Creative Commons Attribution - NonCommercial 4.0 International License

1 **Effect of drying temperature on the properties of alkali-activated binders -**

2 **Recommendations for sample preconditioning**

3
4 Vincent TRINCAL^{1*}, Virginie BENAVENT¹, Hugo LAHALLE¹, Bastien BALSAMO¹, Gabriel SAMSON¹,
5 Cédric PATAPY¹, Yoann JAININ², Martin CYR¹

6
7 ¹LMDC, INSAT/UPS Génie Civil, 135 Avenue de Rangueil, 31077 Toulouse cedex 04 France.

8 ²Ecocem Materials, 4 Place Louis Armand, 75012 Paris, France.

9 *Corresponding author: vincenttrincal @ gmail.com

10
11 **Abstract**

12
13 Various durability tests require a drying step to remove free water without altering the chemistry or
14 microstructure of the materials. However, little is known about the effects of drying on alkali-
15 activated materials (AAMs). This study focusses on the drying stage to assess the behaviour of four
16 alkali-activated binders compared with conventional binders: a metakaolin-based geopolymer,
17 ground granulated blast-furnace slag (GGBS) activated by sodium silicate or by sodium carbonate,
18 and a mixture of metakaolin-GGBS activated by sodium silicate. After a 28-day autogenous cure,
19 mortar and paste samples were dried at temperatures ranging between 20°C and 125°C. Micro-
20 structural damage was observed in metakaolin-based AAMs dried at temperatures above 40°C, but
21 occurred only between 40 and 60°C for GGBS-based AAM. SEM observations and MIP porosimetry
22 coupled with mineralogical analyses, allowed AAMs drying mechanisms to be better understood, and
23 recommendations to be made for the preconditioning of these materials.

24
25
26 **Keywords**

27

28 Alkali-activated binder, Geopolymer, GGBS, Metakaolin, Drying conditions, Preconditioning

29

30 **1. Introduction**

31

32 Alkali-activated binders are produced from a source of aluminosilicates (precursor) mixed with a
33 highly alkaline solution (most of the time either sodium (Na) or potassium (K) silicate solutions, but
34 sometimes hydroxide, carbonate or lithium alkali solutions) called the activating solution [1,2]. There
35 are two main types of alkali-activated binders, differentiated by their precursors' calcium contents,
36 the chemical mechanisms that take place upon hydration and eventually the reaction products. For
37 precursors with low calcium content, such as metakaolins and type F fly ashes, the term geopolymer
38 is used [1]. The chemical reactions contribute to a dissolution/polycondensation process, leading to a
39 3D-aluminosilicate network [3]. For precursors rich in calcium, such as ground granulated blast-
40 furnace slag (GGBS), the reaction process consists of dissolution/precipitation reactions. The main
41 reaction products are C(-A)-S-H type phases ($\text{CaO-Al}_2\text{O}_3\text{-SiO}_2\text{-H}_2\text{O}$) [4].

42

43 Abundant literature is available regarding AAMs formulation, but only a few studies deal with their
44 durability (see reviews by [5–9]). Until recently, to test the durability of AAM matrices, protocols
45 defined for “conventional” binders have often been used, without focusing on protocol impact (in
46 particular of pre-conditioning or drying on the binder structure) or analyses representativeness
47 [10,11]. However, appropriate preconditioning procedures must be selected to avoid potentially
48 misleading conclusions regarding general indicators as well as long-term in-service performance [10–
49 12]. Tests proposed in the literature (see, for example, RILEM framework publications [13,14]) usually
50 require a preconditioning of the specimens, especially a drying step at temperatures ranging from
51 45°C (e.g. accelerated carbonation XP-P-18-458, 2008), to 80°C (e.g. gas permeability XP-P-18-463,
52 2011), or even to 105°C (e.g. porosity NF-P-18-459, 2010). Associated with temperature, the relative

53 humidity can also be fixed for sample preconditioning, e.g. at $57 \pm 3\%$ (SIA 262-1, 2013) and higher
54 than 95% (NF EN 12390-2, 2019). Testing procedures should be reviewed considering the chemical
55 and microstructural properties of the AAM, in order to separate microstructural changes caused by
56 preconditioning (drying) from inherent characteristics (properties and specific microstructural
57 development mechanism) of the material [5,7,8,13,15–17].

58

59 Drying is thus useful to empty the porosity, as well as to stop ongoing hydration of hardened cement
60 paste [18]. The difficulty of drying is to remove as much free water from the pore space as possible
61 (otherwise known as pore water or capillary water) and, at the same time, as little interlayer water
62 (also known as gel water) and as little chemically bound water as possible [18,19]. Desaturation,
63 desorption, and dehydration phenomena associated with drying may generate damage like
64 microcracking, capillary porosity evolution, collapse of fine pores, or mineralogical transformations
65 [20]. The water should thus be removed without damaging the pore structure by capillary hydrostatic
66 stresses due to receding water menisci [19], and without creating any modification of the porosity-
67 mineralogical phases organization.

68 Drying can distort chemical and microstructural interpretations [21,22] so the pre-processing
69 technique used must be considered [23]. Unfortunately, the ideal drying technique, which would
70 preserve the microstructure and remove only the non-bound water, does not exist. All
71 conventionally used drying techniques (e.g. oven, microwave, vacuum drying, D-drying, P-drying,
72 freeze drying and solvent exchange methods) affect the microstructure in their own ways
73 [20,22,24,25]. Removing water without changing the specimen's microstructure and chemical
74 composition is extremely difficult or impossible to accomplish [23]; therefore, a choice has to be
75 made according to the drying objectives [22,26,27]. Finally, all the direct drying methods remove only
76 water without the ions dissolved in the pore solution, which can lead to artefacts, such as the
77 formation of salts during drying [28].

78

79 Many studies have compared the effect of different drying methods on OPC-based cements
80 [12,19,22,23,29,30], but very few have been carried out on alkali-activated binders (e.g. [12,17]).
81 Zhang et al. [12] showed that the porosity of an AAM (based on metakaolin, fly ash and slag activated
82 with sodium silicate solution) can be affected by drying at 65°C under vacuum, and by drying at
83 105°C in an oven. For these authors, low-calcium precursors (geopolymers) are less sensitive to the
84 drying than the higher-calcium one (with GGBS). Their hypothesis is that the thermal stability of the
85 geopolymeric gel is higher than that of C(-A)-S-H, but it can also be added that a smaller proportion
86 of the mixing water is chemically bound in geopolymer than in GGBS-binder, and that the pore
87 networks of these two types of materials differ considerably. Regarding the activator, based on a few
88 precursors, Kovtun [17] showed that sodium metasilicate alkali-activated concrete appears to be
89 more sensitive to drying than a sodium hydroxide-based one. However, due to the great variability of
90 alkali-activated mixtures, as well as the singular behaviour of each of them, it seems delicate to make
91 general remarks on the best method to use to dry all alkali-activated binders. It appears more
92 appropriate to continue the investigations and give recommendations relating to precursor-activator
93 couples.

94

95 The aim of this study is to evaluate the impact of drying on alkali-activated binders for temperatures
96 ranging from 20°C to 125°C. The effect of drying time, primary vacuum and relative humidity content
97 was also evaluated for some samples. For this study, four alkali-activated binders were compared
98 with conventional binders based on OPC (CEM I) and OPC-GGBS (CEM III/B): a geopolymer (sodium-
99 silicate activated metakaolin), a sodium-carbonate activated GGBS, a sodium-silicate activated GGBS,
100 and a sodium-silicate activated mixture of 50 % metakaolin and 50 % GGBS. Pastes and mortar
101 samples were first cured in autogenous conditions at 20°C for 28 days, and then dried in an oven
102 until their mass stabilized.

103 First, the masses of the mortars were monitored during drying in order to assess the water loss of the
104 materials. On these samples, non-destructive testing (NDT) was carried out before and at the end of

105 drying, as acoustic wave propagation velocity and electrical resistivity measurements. Then,
106 destructive analyses (compressive strength and mercury intrusion porosimetry (MIP)) were
107 performed on dried samples and on autogenous ones having the same age. Finally, to better
108 understand a possible evolution of the phase assemblage generated by drying, X-ray diffraction,
109 infrared spectroscopy and thermogravimetric analysis were performed on dried paste samples. All
110 these data allow us to evaluate the effect of drying on the mechanical and microstructural properties
111 of AAMs, and to discuss AAM drying recommendations for durability testing.

112

113

114 **2. Material and methods**

115

116 **2.1. Raw materials**

117

118 Six mixtures were prepared in this study, two conventional binders based on OPC (CEM I) and OPC-
119 GGBS (CEM III/B) and four alkali-activated binders. The choice of the two OPC-based references was
120 justified by the fact that AAMs are potentially intended for the same applications as OPC-based
121 materials, and that there is much more data available on their drying (e.g. [12,19,22,23]).

122 The reference binders used in this study were, following European standard nomenclature (NF EN
123 197-1, 2012), a CEM I (CEM I 52.5 R CE CP2 NF) cement from Lafarge-Holcim (Le Teil, France) and a
124 CEM III/B (42.5 N – LH/SR CE PM NF) cement from Lafarge-Holcim (La Malle, France), which
125 contained 71% of GGBS. Chemical composition was measured by ICP-OES (Perkin Elmer) (Table 1;
126 [31]).

127 For alkali-activated materials, metakaolin (Mk) precursor was manufactured by Argeco
128 Développement (Fumel, France) by flash calcination of kaolinite, i.e. a few seconds at a temperature
129 close to 700°C (see calcination details for this metakolin in San Nicolas et al. [32]). It contained mainly
130 an amorphous metakaolinite phase and crystalline quartz, together with minor mineral phases such

131 as calcite, kaolinite, illite, mullite hematite and rutile (Table 2). The fact that there is more than 40 %
132 of quartz in the metakaolin, of size less than 100 μm , makes the sample of geopolymer paste not
133 really a paste but more like a 'mortar' with quartz fines. Chemically, metakaolin was composed of
134 approximately two-thirds of SiO_2 and one-third of Al_2O_3 , with a few percent of Fe_2O_3 (Table 1). Its
135 density was 2.59 g/cm^3 and its specific surface area was $17 \text{ m}^2/\text{g}$ (BET analysis carried out at the
136 CIRIMAT laboratory, using a Micromeritics Tristar 3020 apparatus with a degassing temperature of
137 350°C).

138 GGBS precursor was manufactured by Ecocem (Fos-sur-Mer, France). It was >95% amorphous slag
139 with a basicity index CaO/SiO_2 of 1.2 (Table 1), a density of 2.93 g/cm^3 , a Blaine specific surface area
140 of $4633 \text{ cm}^2/\text{g}$ and a 28-day activity index of 98% (NF EN 196-1, 2016).

141

142 Alkali-activated materials were prepared from a mixture of metakaolin and/or GGBS with sodium
143 silicate solution or sodium carbonate powder. The sodium silicate was a commercial activation
144 solution (Betol[®] 47T), from Woellner. It contained 55.5% by weight of water and 44.5 % of activator
145 with an $\text{SiO}_2/\text{Na}_2\text{O}$ ratio of 1.7, i.e. 27.5 % of SiO_2 and 16.9 % of Na_2O . Sodium carbonate was a >99%
146 pure Na_2CO_3 powder with a density of 2.53 g/cm^3 from Solvay. Finally, tap water and standard quartz
147 sand (0-2 mm) were used to prepare mortars according to the NF EN 196-1 (2016) mixing protocol.

148

149 **2.2. Sample preparation**

150

151 Four alkali-activated mortars with a water/binder (w/b) ratio of 0.4 were studied (see Table 3). W/b
152 ratio was calculated from the sum of both the added water (tap) and the water of the activation
153 solution, all divided by the sum of the activators' and precursors' dry masses. The first mixture was a
154 metakaolin-based geopolymer developed by the LMDC laboratory. This mixture has been the subject
155 of several publications, for example about formulation and performance [33,34] or robustness [35].
156 Two mixtures of activated GGBS were prepared, one with sodium carbonate activating solution and

157 one with sodium silicate (GGBS-carbonate and GGBS-silicate). Finally, a mixture of 50% metakaolin
158 with 50% GGBS activated by sodium silicate was assessed in this study (Mk-GGBS-silicate) to evaluate
159 the coupling of the two precursors. In order to better identify the crystalline phases in the mortars,
160 four paste mixtures were made, respecting the same raw material and water/binder ratios.
161 Practically, the mixtures were the same as those described for the mortars (Table 3) but without the
162 sand. OPC-based references were composed of mortars made from one CEM I cement and one CEM
163 III/B cement with a water/binder ratio of 0.5 (see Table 3) to obtain a similar consistency as assessed
164 by slump test with a small Abrams cone (height: 15 cm, diameters: 5 cm and 10 cm).

165

166 The mortar mixtures were made in a standardized mixer (Automix Control®) according to standard
167 protocol (i.e. 60 seconds at 140 ± 5 rpm with sand addition after 30 seconds, 30 seconds at 285 ± 10
168 rpm, 90 second pause, 60 seconds at 285 ± 10 rpm, NF EN 196-1, 2016). The activator was first
169 homogenized with water, then the precursor was introduced at the start of mixing, 30 seconds
170 before the addition of sand. Mortars were cast at 20°C into 4x4x16 cm³ polystyrene moulds,
171 protected by films to prevent drying. The test pieces were cast in two steps followed by 10 seconds
172 of vibration on a vibrating table. Most of the samples were demoulded 24 hours after casting, with
173 the exception of the GGBS-carbonate mixture, which was demoulded at 48 hours because of its low
174 mechanical properties at early age. The specimens were then autogenously cured (wrapped in plastic
175 film and sealed in humidified plastic bags) for 28 days at 20°C. After this cure, some samples were
176 kept in autogenous conditions, others were dried at 20°C with several relative humidity values (0% in
177 vacuum dryer in air-conditioned room, 50% in air-conditioned room or 95% in wet room with
178 permanent showers), and the last samples were dried in an oven at 40°C, 50°C, 60°C, 80°C, 105°C or
179 125°C with no control of relative humidity. Note that the temperature in the wet room may have
180 varied between 14 and 25°C. Pastes were made with a KENWOOD kitchen mixer according to the
181 following protocol in five steps: liquid mixing for 2 min at slow speed, addition of powder, mixing for
182 1 min at slow speed and 1 min at fast speed, pause for 30 s, and mixing for 1 min at fast speed. The

183 pastes were cast into 4.5x7.5x2.5 cm³ airtight plastic boxes for an autogenous cure of 28 days, then
184 dried or kept in autogenous conditions.

185

186 **2.3. Methods**

187

188 **2.3.1. Drying kinetics**

189

190 The mortar bars were weighed at a precision of 0.01 g immediately after unmoulding (one or two
191 days after casting), at the end of the 28-day autogenous cure, and several times a week during
192 drying. When the mass had been stable for more than one week (mass loss less than 0.05 % in 7
193 consecutive days), the specimens were considered dry (large dots in Figure 1) and were then
194 analysed using the methods described below. As drying at 125°C was faster than at 80°C, and drying
195 at 80°C was faster than at 40°C, the test samples having undergone these treatments were not
196 analysed at the same age (ages will be systematically specified). Due to the very long drying, it was
197 decided to stop the drying step of samples stored at 20°C - 50 %RH after 7 weeks, and thus before
198 mass stabilization. For the evaluation of drying kinetics, at least 4 samples were analysed for each
199 condition and for each AAM material, but only two samples were analysed per condition for the
200 reference OPC-based cement mortars.

201

202 **2.3.2. Ultrasonic pulse velocity (UPV)**

203

204 A non-destructive method was used to measure the ultrasonic pulse velocity (UPV), i.e. the
205 propagation velocity of an electro-acoustic longitudinal wave (ultrasonic) in the mortars (EN 12504-4,
206 2005; ISO 1920-7, 2004). The machine used was a PUNDIT (Portable Ultrasonic Non-destructive
207 Digital Indicating Tester), from Controlab Proceq, equipped with two P-wave transducers (54 kHz Ø

208 50 mm x 46 mm). Grease was used to make the contacts between the transducers and the 4x4x16
209 cm³ mortar sample.

210 The ultrasonic pulse propagates through the gaseous, liquid and solid phases at 330 m.s⁻¹, 1480 m.s⁻¹
211 and from 2000 to 8000 m.s⁻¹, respectively (e.g. 5500 to 6000 m.s⁻¹ in quartz; [36,37]). In mortar, the
212 UPV depends on several parameters ([38] and reference therein), such as the density and porosity of
213 material [39–42], the degree of saturation of the porosity [43–46], the mechanical strength
214 [41,47,48], microcrack formation [49,50], and temperature [51]. According to the mix design, the
215 UPV of cementitious material lies globally in the 3000 and 5000 m.s⁻¹ range [46,52,53].

216 The UPV analyses carried out in this study were intended to follow the evolution of the mortars
217 under autogenous conditions as well as to non-destructively characterize the evolution of mortar
218 properties caused by drying. In order to limit the amount of data and associated figures, the UPV
219 results are not displayed in the main text but are presented in Supplementary data BS2.

220

221 **2.3.3. Electrical resistivity (r)**

222

223 The resistivity / electrical conductivity of a mortar, which may be related to porosity and water
224 content [54–56], was also measured by a non-destructive, method. According to availability, two
225 machines were used: the first was an Ohmega resistivity meter, from Allied Associates Geophysical
226 Ltd, working in resistance mode at I = 0.5 mA; the second was an assembly consisting of an AC
227 generator operating at 1488 Hz, a voltmeter and an ammeter. The contact between the 4x4x16 cm³
228 mortar specimen and the two electrodes fixed on metal grids was made with a wet sponge, the
229 resistance of which (without sample) was also measured. Mortar bar resistivity (r) is given by
230 Equation 1.

231

$$232 \quad r = R \times S / L \quad \text{and} \quad R = U / I \quad (1)$$

233 with resistance $R = R_{\text{mortar}} - R_{\text{sponge}}$ (resistance of mortar and sponge, respectively); U: voltage in volts;
234 I: intensity in amperes; S: contact surface area in square metres and L: length of the sample in
235 metres.

236

237 **2.3.4. Compressive strength (f_c)**

238

239 A standardized 3R press was used for the mortar 4x4x16 cm³ bar compression tests based on
240 standard NF EN 196-1 (2016). Three tests in compression were performed for each sample instead of
241 one test in bending and two tests in compression. All data are reported in Supplementary data A but
242 only the average of these three results is shown in the figures of this article. Measurements were
243 carried out on dry specimens and on control specimens stored under autogenous conditions for the
244 same duration. In order to evaluate the dispersion of data, at least two specimens were analysed per
245 drying condition for each mortar mixture (i.e. ≥ 6 measurements).

246

247 This destructive test method was coupled with non-destructive testing: acoustic wave propagation
248 velocity and electrical resistivity (Supplementary data A; BS2). All these methods were carried out
249 periodically on mixtures stored in autogenous conditions and on dried samples at the end of drying.
250 The results are intended to complement the data on kinetics and efficiency of drying in order to
251 specify the impact of drying on the materials concretely, and also to refine our hypotheses
252 concerning the mechanisms involved.

253

254 **2.3.5. Bulk density (ρ)**

255

256 Autogenous and dried samples were placed in a desiccator under vacuum for 4 hours. Water was
257 then injected into the desiccator to fully immerse the samples for 24 hours (with the vacuum
258 maintained). Each soaked sample was then weighed under water (hydrostatic weighing M_{water}) and in

259 the air after being wiped (M_{air}). The samples were next dried for one week at 105°C to remove all
260 water then weighed (M_{dry}). This protocol is described in more detail in the standard AFPC-AFREM
261 (1997).

262 The apparent bulk density (ρ) was expressed in $\text{g}\cdot\text{cm}^{-3}$ following Equation 2, where ρ_{water} is the
263 density of water, equal to $0.998 \text{ g}\cdot\text{cm}^{-3}$ at 20°C.

264

$$265 \quad \rho = \frac{M_{dry}}{(M_{air} - M_{water})} * \rho_{water} \quad (2)$$

266

267

268 **2.3.6. Mercury injection porosimetry (MIP)**

269

270 An AutoPore IV 9500 Porosimeter from Micromeritics was used up to a maximum mercury pressure
271 of 400 MPa following the ISO 15901-1 (2005) standard. This allows information to be obtained on
272 pore access diameters (throat-sizes) from 300 μm down to 3 nm, following Washburn's law with a
273 mercury contact angle of 130° and a surface tension of $0.485 \text{ N}\cdot\text{m}^{-1}$ [57]. The samples were not dried
274 again for the MIP analysis, in contrast to what is often recommended but is not mandatory [58].
275 Pieces of mortar of about 1 to 3 g per test were thus put directly into the penetrometer, and then
276 dehydrated during the evacuation step in the porosimeter. Autogenous samples containing water
277 were therefore dried during the evacuation step in the porosimeter, with a risk of this evacuation
278 step inducing an additional modification of the pore network. The test did not start until the exhaust
279 pressure was $\leq 50 \mu\text{mHg}$ (6.666×10^{-5} Bar) assuming complete evaporation of the free water. A test
280 carried out on two geopolymers mortar samples removed from the penetrometer at the end of the
281 vacuum, then placed at 105°C for 24 hours, confirmed that 80-90% of the mixing water had already
282 been removed during vacuuming. Moreover, if a little free water, defined as that being linked to the
283 rigid skeleton only by weak capillary forces, were to remain, the weakness of the capillary forces

284 should not hinder the passage of mercury [59]. For autogenous samples, the evacuation step could
285 therefore last several hours. It was much quicker for previously dried samples.

286

287 It has been demonstrated that, if large pores are accessible by small throats, the mercury forced into
288 the pore remains in it after the mercury pressure is decreased to atmospheric pressure [60]. This
289 phenomenon, called trapping, was exploited by performing MIP analyses in two phases on our
290 samples: intrusion and extrusion. MIP porosity ϕ and the pore size distribution, or more exactly pore
291 access diameter distribution, were also evaluated. For that, in each analysis the intrusion volume was
292 divided into several pressure groups, corresponding to pore size accesses of < 10 nm, 10-100 nm, 0.1-
293 1 μm , 1-10 μm , 10-100 μm and > 100 μm as in [61]. Finally, the pore diameter that we noted $d_{\text{Hm}1}$,
294 corresponding to half the volume intruded in the main intrusion peak (in nm) was evaluated. The
295 objective of this indicator is to observe the evolution of the size of the finest pores (in the main
296 intrusion peak), without being influenced by microcracking.

297

298 The notion of free and trapped porosities is not often used in civil engineering publications [62,63].
299 To summarize, the mercury intrusion allows the total connected porosity to be calculated. When the
300 pressure returns to atmospheric pressure, part of the mercury remains trapped in the sample
301 corresponds to the trapped porosity, it is represented by pore-throat arrangements with low throat-
302 to-pore-size ratio. Analogously, voids with high throat-to-pore-size ratios, including cracks, are free of
303 mercury at this stage since they do not entrap it [60]. By carrying out different cycles of intrusions
304 and extrusions, Portsmouth and Gladden [64] and Mata et al. [65,66] saw that the volume of
305 mercury looped on the same hysteresis cycle, which characterized the possibilities of privileged
306 transfers within the porous system. The percentage of trapped mercury can be qualitatively
307 correlated with the degree of porous network connectivity (α) (equation 3): the weaker α is, the
308 more the material will be connected. Permeability is a complex notion determined by the ink-bottle
309 effect, the size of the different pore families, and also the tortuosity and connectivity of the material.

310 Knowing the degree of connectivity of the pores (equal to the ratio of volume of mercury extruded to
311 volume of intruded mercury) therefore makes it possible to understand some of the permeability
312 properties of the material.

313

$$314 \quad \alpha = \frac{\text{Volume of extruded mercury}}{\text{Volume of intruded mercury}} \quad (3)$$

315

316 Due to the toxic and polluting characteristics of mercury and the complex management required for
317 the contaminated samples after testing, only one analysis was conducted for each binder, drying and
318 age. However, to verify the repeatability, several duplicates were analysed on some samples. In this
319 case only the average and the confidence interval are displayed in the graphs.

320

321 **2.3.7. Scanning Electron Microscopy (SEM)**

322

323 Paste materials were observed with a JEOL JSM 3680 on polished surface. Cubic 1x1x1 cm³ SEM
324 samples were broken or cut from the paste samples with a circular saw. Samples were polished with
325 ethanol using carbide polishing disks (Presi) (polishing discs and grain size: ESCIL, P800–22 µm,
326 P1200–15 µm and P4000–5 µm). Then samples were coated with graphite and placed in the SEM
327 chamber until a vacuum of 2.10⁻⁵ mBar was reached. Mineralogical phases and cracks were observed
328 in backscattered electron detection mode.

329

330 **2.3.8. X-Ray Diffraction (XRD)**

331

332 Alkali-activated pastes were crushed manually in an agate mortar until a powder with particles < 40
333 µm (sieve control) was obtained. The diffractometer was a Bruker D8 Advance using a copper X-ray
334 tube, equipped with a vertical theta / theta goniometer and a LynxEye XE-TTM high-speed linear
335 detector. A motorized anti-scattering knife was used. The acquisition of the diffractograms was

336 carried out at 40 kV and 40 mA, from 7° to 70° 2θ with an interval of 0.02° 2θ and a total acquisition
337 time of 2h30 per sample. Minerals were identified using the Bruker-AXS DIFFRACplus Eva v4 software
338 and the 2015 ICDD PDF database. Metakaolin mineralogical quantification was performed by Rietveld
339 calculation with DIFFRACplus Topas v5 following rules described in Trincal et al. [67].

340

341 **2.3.9. Fourier-transform infrared spectroscopy (FTIR)**

342

343 FTIR analyses were performed using a Perkin Elmer Frontier FTIR spectrometer. The analyses were
344 made on a layer of crushed paste (< 80 μm) directly deposited on the diamond cell after measurement
345 of the background in the air. The transmittance spectrum obtained was an accumulation of 12
346 measurements made between 4000 cm⁻¹ and 600 cm⁻¹.

347

348 **2.3.10. Thermogravimetric analysis (TGA)**

349

350 The TGA method quantified the mass losses of a sample undergoing a temperature increase in a
351 controlled atmosphere, in order to identify the chemical reactions or the phase changes that possibly
352 occurred in the sample under heating [68,69]. Analyses were carried out using a Mettler Toledo TGA2
353 STAR[®] system. For each sample, approximately 0.5 g of paste powders (< 80 μm) was heated in a 150
354 μL crucible, from 25 or 30°C to 1050°C with a ramp of 10°C/min under 50 mL/min of Argon.

355

356 **3. Mortar characterization results**

357

358 **3.1. Water loss kinetics**

359

360 Figure 1 shows the mass variations recorded during the different drying processes for the six
361 mixtures, and Figure 2 reports the water content (V_w) of the mortars at the end of drying. For both

362 figures, dot and histogram colours are related to the temperature used for drying. It can be seen
363 that, for both alkali-activated and OPC-based mixtures, the higher the temperature, the faster and
364 more effective the drying process. These results follow exponential decrease laws and are consistent
365 with the literature [23]. For instance, at 105°C and 125°C, 4x4x16 cm³ mortar bars were considered
366 fully dried after 2 or 3 days, while it was necessary to wait for about two or three weeks at 40°C to
367 obtain mass stabilization, and almost two months at 20°C - 50 %RH (Figure 1). According to Kelvin's
368 law at 20°C [70], the lower the relative humidity, the smaller the Kelvin radius (r_k) [71]. When the
369 radius of a pore is higher than the r_k , it desaturates. In the case of the geopolymer [72], $r_k = 51.97$ nm
370 for RH = 98%, 1.7 nm for RH = 54% and 0.95 nm for RH = 33%. The relative humidity was not
371 controlled during oven drying. However, the geopolymer pore size was larger overall than in CEM- or
372 slag-based mixtures, suggesting that, for a fixed humidity, the geopolymer will desaturate more
373 quickly. It is therefore likely that temperature, relative humidity and pore size have a combined
374 effect on drying kinetics.

375

376 Whatever the conditions, geopolymer and Mk-GGBS-silicate masses stabilized faster than those of
377 the other four mixtures, suggesting higher water transfer properties. This is supported by the facts
378 that the pore size varies according to the mixture, and that free water is more easily removed than
379 chemically bound water. In geopolymer, there is mostly free water [3,73], while in CEM- or slag-
380 based binders a large proportion of the water is physically absorbed and chemically bound in
381 hydrates. To go further, the nature of hydrates is not the same in cement-based mortars as in those
382 based on slag, and GGBS-OPC binders are known to have smaller pore size distributions than pure
383 OPC. The chemical bonds between water and hydrates are therefore not the same, which can
384 contribute to different drying kinetics. At the end of the autogenous cure, depending on the amount
385 of air bubbles trapped during mixing, the degree of saturation of geopolymer porosity is close to 95-
386 100% [72], while it is much lower in the other binders (water was emptied from the pores during

387 hydration). This is confirmed by the mass increase of cementitious and slag mortars when they are
388 placed in the wet room, corresponding to a re-saturation of the porosity (Figure 2).

389

390 **3.2. Strength properties**

391

392 Figure 3 shows the compressive strength (f_c) of the four alkali-activated and the two CEM-based
393 mixtures. In this figure, the dot colour is related to the temperature (as in previous figures); the
394 vertical axis corresponds to the duration of drying (after 28 days under autogenous conditions) and
395 the horizontal axis to mechanical strengths in MPa.

396

397 - Geopolymer stored in autogenous conditions had similar f_c values from 28 to 150 days (Figure 3A;
398 Supplementary data A). Without water exchange, the geopolymer strength no longer evolved once
399 the geopolymerization reactions were completed. Both ultrasonic pulse velocity (UPV) and resistivity
400 results were also constant between 28 and 88 days (Supplementary data B), confirming that there
401 was no material damage or evolution during this period. All these results are consistent with the
402 literature, since most geopolymerization reactions take place in the first few days after casting
403 [33,74].

404

405 After 28 days of autogenous cure, geopolymer dried at a temperature $\geq 50^\circ\text{C}$, and especially between
406 80°C and 125°C , induced a large f_c loss (of as much as 37 %; Figure 3A; Supplementary data A). This
407 loss persisted with an extension of drying for several weeks (e.g. same f_c for samples dried for 14 or
408 60 days at 105°C). For drying at $T \leq 40^\circ\text{C}$, the dried geopolymer samples showed similar f_c to those
409 stored in autogenous conditions. The UPV values of the geopolymer seemed to be modified in
410 proportion to the intensity of drying. Samples cured in a wet room had identical results to
411 autogenous samples of the same age. Samples dried at temperature $T \leq 40^\circ\text{C}$ showed a very slight

412 decrease in UPV, and in those dried at $T \geq 60^\circ\text{C}$ UPV dropped by about a quarter (Supplementary
413 data A; BS2).

414

415 Significant similarities observed between the UPV and f_c trends suggest a relationship between them,
416 and the possibility of evaluating geopolymer f_c with non-destructive UPV measurements. However,
417 this implies a calibration step to assess the contribution of each parameter: the porosity and its
418 degree of saturation, the microcrack occurrence, the mineralogical assemblage, etc. (see part 1.4.
419 Methods).

420

421 - GGBS-silicate and GGBS-carbonate conserved in autogenous conditions underwent a slow strength
422 increase from 28 to 88 days, and seemed stabilized beyond 6 months (Figures 3B and 3C;
423 Supplementary data A). Resistivity was 10 times higher than in the geopolymer and this value
424 increased over time (Supplementary data BS4). The resistivity of a material depends, among other
425 things, on its water content (open porosity and degree of saturation of the pores) and the
426 concentration of salts in the porous solution [56]. Resistivity increase in autogenous conditions can
427 thus be related to the continuation of hydration reactions over time through the consumption of
428 water or ions by the pores, also leading to strength increase. For these two mixtures, ultrasonic pulse
429 velocity values were stable over time, as for geopolymer but with higher values. The speed of
430 propagation of an electro-acoustic longitudinal wave depends on the properties of the medium it
431 crosses, which suggests that the two GGBS-based mixtures were denser and more rigid/less porous
432 than the geopolymer [38]. The geopolymer bulk density of 2.01 g.cm^{-3} was indeed lower than those
433 of GGBS-silicate and GGBS-carbonate, with 2.16 g.cm^{-3} and 2.11 g.cm^{-3} , respectively (Table 3).

434

435 For both mixtures, drying at $T \geq 80^\circ\text{C}$ or at 20°C (whatever the humidity), did not decrease the f_{cs} ,
436 which were similar to those of samples stored under autogenous conditions (Figures 3B and 3C).
437 However, drying at 60°C or, more significantly, at 40°C decreased the f_c by as much as 36 % and 24 %

438 for GGBS-silicate and GGBS-carbonate, respectively. This was not due to the time spent in the oven
439 since the samples kept in the oven for 2 months showed results similar to those analysed at the end
440 of regular drying. Further drying at 40°C - 80% RH was carried out on the GGBS-silicate. The results
441 were similar to those of autogenous samples, i.e. almost no water flow or strength modification,
442 suggesting that the temperature of 40°C affects the f_c only when humidity is low.

443

444 - Mk-GGBS-silicate stored in autogenous conditions showed a marked f_c increase between 28 and 88
445 days (Figure 3D; Supplementary data A). Ultrasonic pulse velocity results revealed an augmentation
446 over time in autogenous conditions while resistivity remained constant (Supplementary data A, BS2).
447 This suggests an increase in the density or rigidity of the material, without any drastic modification of
448 the pore solution. However, the bulk density remained constant at 2.08 g.cm⁻³ (Supplementary data
449 BS1). These results suggest a combination of several reactions over time, such as hydration reactions
450 in the unreacted slag and recrystallization/restructuring of the geopolymeric gel.

451

452 Surprisingly, whatever the temperature used, the Mk-GGBS-silicate drying considerably reduced both
453 f_c (by between 30% and 45%) and UPV (by 25%) (Figure 3D; Supplementary data A, BS2). Only
454 samples cured in the wet room (20°C - 95% RH) presented results similar to those of autogenous
455 samples. Once dry, samples no longer showed f_c increases – unlike the autogenous one, in which the
456 f_c difference increased over time. This suggests that even the smallest loss of water caused by drying
457 at 20°C - 50 %RH, is enough to stop the chemical reactions, an observation that is probably related to
458 a humidity drop in the mortar. Other possibilities are development of cracking or even structure
459 degradation due to removal of water from the skeleton. This mixture thus seems very sensitive to the
460 evaporation of its water, more than geopolymer, despite very close water contents.

461

462 - The f_c s of CEM I and CEM III/B mortars were very stable over time between 28 and 88 days in
463 autogenous conditions (Figures 3E and 3F). Furthermore, neither of these two mixtures showed an f_c

464 drop due to drying. In contrast, CEM III/B showed an f_c increase of about a third for a drying
465 temperature $\geq 80^\circ\text{C}$, which was probably related to an acceleration of hydration reactions by the
466 thermal curing [75,76]. On CEM III/B concrete samples, Azar et al. [77] observed an f_c increase of 15
467 % with drying at 40°C .

468

469 **3.3. Porosity**

470

471 Mercury intrusion porosimetry (MIP) data are reported in Table 4 and illustrated Figure 4. For each
472 AAM, Table 4 gives three parameters: the connected total porosity (ϕ) in %, the degree of pore
473 connectivity (α) in %, and the pore diameter (d_{Hm1}) in nm corresponding to half of the mercury
474 volume intruded in the main intrusion peak. According to the pore size distribution (supplementary
475 data BS5), the main intrusion peak was bounded between 3 and 1000 nm for geopolymer, and
476 between 3 and 225 nm for all other AAMs. All the larger pores (i.e. > 1000 nm or > 225 nm,
477 respectively) appear to have been formed by microcracking due to preconditioning and were not
478 integrated in the d_{Hm1} parameter. All ϕ , α and d_{Hm1} data are given according to drying and time (0
479 corresponds to the end of the cure, i.e. after 28 days in autogenous conditions, when samples were
480 placed in drying or maintained in autogenous conditions). The reason why there is no confidence
481 interval given in Table 4 is that only one sample was analysed, as good repeatability had been shown
482 for other samples.

483

484 Figure 4 shows the evolution of the pore access diameter distribution, called pore size distribution, of
485 the four AAM mixtures dried or stored in autogenous conditions. For each mortar analysed, intrusion
486 volume was divided into six pore size groups: < 10 nm, 10-100 nm, 0.1-1 μm , 1-10 μm , 10-100 μm
487 and > 100 μm . To achieve this, the intrusion volume was calculated between the pressure stages
488 corresponding to the sizes of intruded pores as performed in Ortega et al. [61]. We recall that, if it is
489 necessary for the mercury to pass through smaller capillaries to fill large pores (ink bottle effect),

490 then the measurement made by MIP will give a pore access diameter equal to the size of the smallest
491 capillaries [78].

492

493 Geopolymer mortar stored in autogenous conditions has an MIP porosity close to 18 %, which might
494 decrease slightly over time but, due to the accuracy of the measurements, more analyses would be
495 necessary to confirm this trend (Table 4). The pore access sizes distribution is monomodal, centred
496 around 7 nm (Table 4; Supplementary data BS5). Most of the mercury is introduced into samples for
497 pore access sizes between 5 and 20 nm, which corresponds to two categories in Figure 4 (< 10 nm
498 and 10-100 nm). In autogenous conditions, the geopolymer pore size distribution seems to remain
499 stable over time, as confirmed by d_{Hm1} (Table 4). Between 3 and 1000 nm (main intrusion peak), half
500 of the intruded mercury volume corresponds to a pore size $d_{Hm1} = 9$ nm, whatever the autogenous
501 cure duration. These results are consistent with literature data, according to which the pore volume
502 is stable over time and there are two pore families: first, a mean pore size generally close to 5-10 nm
503 depending on the water content, and second a porosity visible at microscale by microscopy but
504 invisible in MIP due to the ink-bottle effect [34,79]. Finally, for these autogenous samples, there is as
505 much free as trapped porosity; the connectivity of the porous network is high (α close to 50%; Table
506 4).

507

508 The more intense the drying, the greater the MIP porosity (up to 23.5 % for drying at 105°C), and the
509 greater the size of the pore accesses (Table 4; Figure 4B). Whatever the conditioning, with the
510 exception of the humid room (at 20°C-95 %RH), which is not a desiccant condition, drying induces an
511 increase in the d_{Hm1} which can be associated to drying shrinkage and formation of microcracks (Table
512 4; Supplementary data BS5). The d_{Hm1} doubles with drying at 20°C, quadruples at 40°C, and is
513 multiplied by ten for a temperature $\geq 80^\circ\text{C}$. This results in a change of the pore size categories in
514 Figure 4B, where, above 40°C, there are no more pores < 10 nm and, above 80°C, the 0.1-1 μm pore
515 category becomes the most abundant. These variations could be the consequence of material micro-

516 cracking and/or the collapse of the walls between the smaller pores. This seems to be confirmed by a
517 slight decrease in α to 44.5 at 125°C (Table 4), suggesting a higher connectivity of the porous
518 network.

519

520 GGBS-silicate and GGBS-carbonate mortars stored in autogenous conditions for more than 28 days
521 were less porous than geopolymer, with total accessible porosities around 12% and 15% respectively
522 (Table 4; Figures 4C; 4E). However, the reproducibility of the analyses was not very good (in
523 particular for GGBS-carbonate with porosity differences of up to 4% between two samples) and the
524 intrusion curves show that these samples were not saturated with mercury. This last point indicates
525 that, unlike in the geopolymer, there were pores smaller than 3 nm. With a different liquid surface
526 tension, the water porosity measurements confirmed MIP data, with GGBS-based mortars having a
527 porosity close to 17 %, compared with 21 % for the geopolymer (Supplementary data BS5). The pore
528 size distribution was monomodal < 30 nm for the GGBS-silicate, with an average d_{Hm1} of 6.5 nm and α
529 close to 67 % (Table 4; Figures 4C). For GGBS-carbonate, the pore size distribution was monomodal <
530 50 nm with an average d_{Hm1} of 9.2 nm and α close to 60 % (Table 4; Figures 4E). Note that, for this
531 last binder, both d_{Hm1} and α seem to have decreased during the autogenous cure. The connectivity of
532 the porous network in GGBS-binder is thus lower than in geopolymer, the pore size is different, as is
533 probably the case for the ink-bottle effect and the tortuosity, so the permeability is very likely to be
534 different between the metakaolin and slag-based binders. This can have repercussions on water
535 transfers and drying kinetics (Figure 1).

536

537 With drying, no mixtures stored at 20°C (at relative humidity of 0 %, 50 % or 95 %) appear to have
538 been significantly affected. The ϕ , α and d_{Hm1} have similar values (Table 4), and the pore size
539 distribution also appears to be identical (Figures 4D; 4F). In contrast, GGBS-binders dried at 40°C or
540 more show a significant increase of the d_{Hm1} , to the extent of being quadrupled. This results in a drop
541 of the pore access category < 10 nm in favour of the 10-100 nm and > 1 μ m ones (Figures 4D; 4F).

542 Regarding the MIP porosity, for GGBS-silicate, ϕ is higher for samples dried at 40°C than for those
543 stored under autogenous conditions, but lower than those dried at $T \geq 60^\circ\text{C}$ (Table 4). For GGBS-
544 silicate, ϕ is higher for samples dried at $T \geq 60^\circ\text{C}$ than for all the others. The connectivity of the pores
545 appears to be maximum for the GGBS-silicate dried at 40°C; while it appears minimum for GGBS-
546 carbonate dried at $T \geq 60^\circ\text{C}$. For these two AAMs, drying at 40°C seems to have different effects from
547 drying at $T > 60^\circ\text{C}$, suggesting micro-cracking formation (as for geopolymer) or assemblage phase
548 transformation.

549

550 Mk-GGBS-silicate mortar stored in autogenous conditions showed a MIP porosity content lying
551 between those of the geopolymer and the GGBS-silicate and decreasing over time (Table 4). The d_{Hm1}
552 was close to 6.8 nm, smaller than the geopolymer value, and the pore access diameter distribution
553 was below 20 nm. According to the intrusion curves, these samples were not saturated with mercury,
554 suggesting a pore size population below 3 nm. By grouping the pore access diameters by classes, half
555 the Mk-GGBS-silicate samples were found to have porosities of < 10 nm at the end of the cure, while
556 this value reached three quarters 6 months later (Figure 4G). Like ϕ , the connectivity of the porous
557 network of GGBS-binder seems to be between those of the geopolymer and the GGBS-silicate.

558

559 With drying, all tested conditions resulted in ϕ , d_{Hm1} and pore connectivity increases (α decrease)
560 (Table 4). This led the pore access diameters category < 10 nm to be replaced by the 10-100 nm one
561 (Figure 4H). This material thus behaves similarly to the geopolymer, despite the fact that the use of
562 slag has reduced its porosity.

563

564 **4. Paste characterization results**

565

566 According to previous results on mortar, AAM pastes may also be affected by drying. Note that for
567 geopolymer and Mk-GGBS-Silicate pastes, the use of a pure metakaolin as raw materials (the used

568 one contains more than 40% of quartz, Table 2) could induce different behaviors. Depending on the
569 mixtures and the temperatures used, several phenomena can come into play: microcracking, phase
570 dehydration, degradation or recrystallization, etc. In order to clarify these hypotheses, paste samples
571 were cast, stored in autogenous conditions then dried before microscopic observations and
572 mineralogical identifications.

573

574 **4.1. Scanning Electron Microscopy (SEM) observations**

575

576 Geopolymer paste stored in autogenous conditions or dried at 40°C showed a network of reticulated
577 cracks, i.e. with primary large cracks (5-10 µm wide) that could be followed over several mm, as well
578 as secondary and tertiary finer cracks (Figure 5A; Supplementary data BS6). These cracks were
579 probably produced by the SEM vacuum [80] and/or by drying shrinkage.

580 Most cracks occurred preferentially at the interface between the geopolymer and quartz grains
581 which were initially present in the metakaolin. On the other hand, only a few cracks appeared
582 between the remaining undissolved metakaolin grains and the geopolymer paste. The geopolymer
583 paste seemed generally unaltered by drying at $T \leq 40^\circ\text{C}$.

584

585 With drying at 60°C (Supplementary data BS6) or 105°C (Figure 5B), the geopolymer microstructure
586 was different. Fewer large cracks were visible, most likely because most of the drying shrinkage had
587 already taken place before SEM sample preparation, during the oven step. The cracks were narrower
588 than in autogenous samples and did not have a reticulated network. The geopolymer paste seemed
589 less dense and less homogeneous (looking more cavernous, corroded, with grain detachment),
590 suggesting that drying at 60°C or more induced a textural modification of the geopolymeric gel,
591 possibly micro-cracking, and an increase of visible porosity.

592

593 GGBS-silicate and GGBS-carbonate pastes seemed to have the same behaviour. In autogenous
594 conditions, as the paste dried for 60 days at 20°C-65% RH, they showed a mosaic of small cracks
595 (Figures 5C) that seemed to form preferentially at the slag/grain interface and were probably caused
596 by desiccation induced by slag hydration (autogenous shrinkage) or desiccation in the vacuum
597 chamber of the microscope [81]. Supplementary, bigger cracks were observed for GGBS-carbonate
598 compared to GGBS-silicate, possibly explained by a greater autogenous shrinkage coupled with the
599 slightly lower strength of the material.

600 With drying at 40°C, 60°C or 105°C, desiccation shrinkage induced large cracks (Figures 5D; 5E; 5F;
601 Supplementary data BS6). A network of secondary cracks was also observable for samples dried at
602 40°C and 60°C (Figures 5D; 5E) but not for the one dried at 105°C (Figure 5F). Drying at 105°C
603 therefore appears to be less damageable than drying at 40-60°C, suggesting that drying intensity and
604 speed have an effect on the GGBS-binder microstructure. Similarly to geopolymer, the paste seemed
605 less dense and less homogeneous after drying.

606

607 Mk-GGBS-silicate paste cured in autogenous conditions presented a network of cracks intermediate
608 between that of the geopolymer and that of GGBS-silicate (Figures 5G; Supplementary data BS6). The
609 micro-cracks crossed the matrix and ran along the grains of quartz and slag, which seems to indicate
610 good grain-matrix cohesion.

611 Whatever the drying temperature (40°C, 60°C or 105°C), the texture of the paste seemed to be
612 affected (Figure 5H) and looked like geopolymer dried above 40°C or the GGBS-silicate at 40°C or
613 60°C. The behaviour of Mk-GGBS-silicate therefore seems to be intermediate between those of the
614 geopolymer and the GGBS-silicate.

615

616 **4.2. Mineralogical analyses**

617

618 X-ray diffractograms of geopolymer kept in autogenous conditions showed a mainly amorphous
619 material with crystallized phases, mainly quartz (SiO_2), and minor phases such calcite (CaCO_3),
620 hematite (Fe_2O_3), mullite ($3\text{Al}_2\text{O}_3 \cdot 2\text{SiO}_2$), anatase and rutile (TiO_2) and other phyllosilicates (kaolinite
621 ($\text{Al}_2\text{Si}_2\text{O}_5(\text{OH})_4$) and illite/muscovite probably ($\text{K}(\text{Al},\text{Mg},\text{Fe})_2(\text{Si},\text{Al})_4\text{O}_{10}[(\text{OH})_2,(\text{H}_2\text{O})]$) (Figure 6A). The
622 FTIR spectrum (Figure 7A) exhibited the asymmetric stretching vibration of Si-O-T bonds (where T is
623 tetrahedral silicon or aluminium related to geopolymeric gel) close to 985 cm^{-1} [82,83], and Si-O out-
624 of-plane bending vibration at 693 cm^{-1} [84]. It also confirmed the presence of carbonate since
625 vibration of O-C-O bonds between 1430 and 1390 cm^{-1} was observed [85]. The TGA spectrum (Figure
626 8A) pointed out three weight losses: a first, main one generally attributed to the loss of water within
627 the porosity of the materials from 80°C to 250°C , a small second one between 300°C and 600°C
628 attributed to the release of water by condensation/polymerization of Si-OH and Al-OH groups, and a
629 third one between 600°C and 800°C related to the decomposition of carbonate species [86].

630

631 Whatever the drying temperature, no mineralogical changes were observed on X-ray diffractograms
632 for geopolymers kept at 40°C , 60°C , and 105°C (Figure 6A). However, the hotter the drying was, the
633 less marked was the amorphous hump. This may have been due to porous solution crystallization
634 during drying or a change in the structure of the amorphous gel as suggested by SEM observations
635 (Figures 5A; 5B). TGA analyses and FTIR spectrum (H-OH peak close to 1646 cm^{-1}) exhibited a
636 decrease of water within the materials, which became greater with temperature (Figures 7A; 8A).
637 Water loss with drying up to 105°C did not seem to change the mineralogy of the geopolymer, as
638 mainly free water in the porosity seemed to be removed. In the TGA spectrum, the decrease in the
639 signal of free water (80 - 120°C) in the porosity revealed the presence of a second signal attributed to
640 physically bound water (150 - 200°C). It might be water bound in the hydration shell of the sodium
641 counter ions [87,88].

642

643 GGBS-silicate autogenous paste diffractograms showed broad peaks (at 20-38° and 49-51°) assigned
644 to amorphous phases and C-S-H / C-A-S-H (PDF file 33-0306; Figure 6B). These identifications were
645 confirmed by Si-O-T bond peaks in FTIR spectra (Figure 7B), and also by weight loss between 105°C
646 (loosely bound water) and 500°C (tightly bound water) on TGA spectra, corresponding to the
647 evaporation of free water and interlayer water, and then the dehydroxylation of C-S-H / C-A-S-H
648 close to 700°C (Figure 8B, [89–91]). Tobermorite ((CaO)_x-SiO₂-zH₂O, PDF file 06-0010) and
649 hydrotalcite (Mg₆Al₂CO₃(OH)₁₆-4H₂O, PDF file 14-0191) (Figure 6B) were observed in our autogenous
650 samples, as cited in the literature [12]. On X-ray diffractograms, we observed that carbonation
651 creating calcite and vaterite (CaCO₃) easily occurred when GGBS-silicate pastes came into contact
652 with air.

653
654 After drying at 40°C for 35 days, 60°C for 24 days or 105°C for 14 days, GGBS-silicate pastes did not
655 show mineralogical changes on X-ray diffractograms. Only a very slight decrease of the main
656 amorphous hump was observed in X-ray diffractogram for 105°C drying (Figure 6B), probably due to
657 dehydration of some C-S-H / C-A-S-H [90,91]. FTIR spectra and TGA thermograms also confirmed that
658 there was no mineralogical modification due to drying, except for a different water loss (Figures 7B
659 and 8B). With drying, less loosely bound water was noticed (up to 200°C) and a little more bound
660 water (up to 500°C), that might be explained by the ongoing hydration of GGBS-silicate pastes over
661 time, and potentially more C-S-H / C-A-S-H phases formed.

662
663 GGBS-carbonate pastes kept in autogenous conditions showed, as for GGBS-silicate samples, the
664 presence of an amorphous hump on X-ray diffractograms, probably related to C-S-H / C-A-S-H phase
665 (Figure 6C). Calcite, gaylussite (Na₂Ca(CO₃)₂·5H₂O, PDF file 21-0343) and hydrotalcite
666 ((Mg_{0.667},Al_{0.333})(OH)₂(CO₃)_{0.167}(H₂O)_{0.5}, PDF file 89-0460) were also detected. In FTIR spectra, the
667 1350-1550 cm⁻¹ band and the shoulder at 871 cm⁻¹ refer to the carbonation products in the paste
668 (Figure 7C; [92]).

669

670 X-ray diffractograms on GGBS-carbonate revealed mineralogical variations after drying, (Figure 6C).
671 With drying at 40°C, gaylussite peaks decreased in intensity and calcite peaks increased, while at
672 60°C and 105°C, there was no more gaylussite and the calcite appeared even more abundant (Figure
673 6C). The increase in calcite, however, was not confirmed by TGA, where the mass loss at around
674 700°C remained similar (Figure 8C). Calcite and hydrotalcite were present in all samples and seemed
675 not to be affected by drying. An evolution of the carbonate compound structures of GGBS-carbonate
676 paste thus seemed to be observed by X-ray diffraction. Like GGBS-silicate, GGBS-carbonate drying led
677 to less loosely bound water being found in TGA analyses, and a little more bound water (Figure 8C).
678 FTIR spectra also attested to the carbonate evolution, where O-C-O bound peaks had very different
679 shapes depending on the drying, especially for drying at temperatures up to 60°C (Figure 7C).

680

681 Mk-GGBS-silicate pastes were a combination of minerals found in geopolymer and in GGBS-silicate
682 pastes. On the X-ray diffractogram, autogenous samples showed an amorphous hump (probably
683 combining geopolymer matrix and C-S-H / C-A-S-H phases), quartz, calcite, hematite, mullite, anatase
684 and other phyllosilicates (kaolinite, illite/muscovite) (Figure 6D). The FTIR spectrum was consistent
685 with the suggested mix of geopolymer matrix and GGBS-silicate matrix, since Si-O-T bands (960 – 967
686 cm^{-1}) were observed between 985 cm^{-1} (geopolymer) and 950 cm^{-1} (GGBS-silicate) (Figure 7D). The
687 TGA spectrum was similar to the geopolymer one but with slightly more water loss between 200°C
688 and 500°C confirming the presence of C-S-H / C-A-S-H phases (Figure 8D).

689

690 Few mineralogical changes were visible after drying. There was a slight decrease in the amorphous
691 hump on XRD diffractograms at 40°C, 60°C or, more significantly, at 105°C, suggesting an evolution of
692 geopolymer matrix and C-S-H / C-A-S-H phases (Figure 6D). Then, FTIR spectra showed slight
693 variations in the O-C-O bond related to carbonates (Figure 7D), which were confirmed by slight
694 variations in the TGA weight loss around 660-680°C (Figure 8D).

695

696 5. Discussion

697

698 5.1. Summary of behaviour of alkali-activated materials under drying

699

700 Most of the data in this article are summarized in Figure 9. They showed that CEM I and CEM III/B
701 mortars were not mechanically damaged whatever the drying temperature (20°C to 105°C). The
702 compressive strengths at each maturity time were equal to the ones of the reference sample kept in
703 autogenous conditions (Figure 3E), and even increased for CEM III/B after drying at 80°C and 105°C
704 (Figure 3F). This was probably related to an acceleration of hydration of slag by thermal curing
705 [75,76]. However, different behaviours were observed for alkali-activated materials (Figure 9).

706

707 For the four alkali-activated materials, the higher the drying temperature was, the faster and the
708 more effective was the drying (Figures 1, 2). Drying the geopolymer and MK-GGBS-silicate at 20°C,
709 40°C and 105°C, removed respectively 50 %, 65 to 68 %, and 80 % of mixing water, while drying the
710 GGBS-silicate and GGBS-carbonate at the same temperature removed 10 to 20 %, 48 to 58 % and 72
711 % of mixing water, respectively (Figure 9A). This lower evaporation rate for slag and cement-based
712 systems can be explained by the smaller pores, which remain saturated and the presence of hydrated
713 phases. In addition, damage in AAMs could be observed to depend on the drying (Figures 9B and 9C):

- 714 - Geopolymer dried at a temperature $\geq 50^\circ\text{C}$, and especially between 80°C and 125°C , induced
715 a significant compressive strength loss (of up to 37 %). This correlated well with a drop of
716 about a quarter in the ultrasonic pulse velocity, which is a technique commonly used to
717 follow the damage evolution in materials [41,47,48].
- 718 - GGBS-silicate and GGBS-carbonate strengths were not affected by drying at $T \geq 80^\circ\text{C}$ or at
719 20°C (whatever the humidity). However, an f_c loss was observed with drying at intermediate
720 temperatures: 40°C and 60°C with low relative humidity. In the meantime, all samples dried

721 at $T \geq 40^\circ\text{C}$ had a large UPV decrease. It is therefore not currently conceivable to assess the
722 strength of GGBS-silicate (unlike geopolymer) materials with this NDT method, but rather to
723 detect the formation of microcracks.

724 - MK-GGBS-silicate was damaged whatever the drying temperature (30% to 45% strength
725 loss), combining the weak points of both geopolymer and GGBS-silicate materials.

726

727

728 **5.2. Mechanisms**

729

730 **5.2.1. Geopolymer**

731

732 No mineralogical changes able to explain the compressive strength losses were detected by visual
733 observation of XRD (Figure 6A), FTIR (Figure 7A), or TGA (Figure 8A), although a decrease in water
734 content was demonstrated with all these methods. A detailed statistical analysis of these spectra
735 could, however, refute this overall interpretation. As it dries, the pore solution should precipitate
736 phases that were not detected in XRD, possibly because they occurred in too small a quantity, or had
737 a composition similar to the gel. SEM observations also showed microstructural modification (Figure
738 5), with a less dense geopolymer paste and the apparition of porous zones. The decrease in strength
739 and the modification of microstructure is consistent with Llyod's work [93] comparing metakaolin-
740 based geopolymer before and after a heat treatment at 95°C . However, contrary to this study, no
741 zeolite was formed in our case after the heat treatment – or the amount formed was too low to be
742 detected by XRD even at 105°C or 125°C . The abundance of quartz in metakaolin could also have an
743 influence on the modification of the microstructure, which could possibly be avoided by using a purer
744 metakaolin as raw material.

745 Nevertheless, SEM observations (Figure 5) showed that drying at 40°C or less induced no visible
746 textural modification of the geopolymeric gel. These observations could be explained by a drying

747 shrinkage which increases as more free water is removed from 20 to 125°C [73,94]. Kuenzel et al.
748 [94] attributed this shrinkage event to capillary strains in the sample following the loss of free water
749 and concluded that the hydration spheres of Na⁺ cations play a significant role in maintaining the
750 structural stability of the paste.

751

752 **5.2.2. GGBS-silicate and GGBS-carbonate**

753

754 For both slag-based AAMs, drying at T ≥ 80°C induced an increase in the pore size (Figure 9E), but did
755 not cause mineralogical change (Figures 6; 7; 8), additional cracking (Figure 5) or significant
756 mechanical strength damage (Figure 9B). Conversely, drying at 40°C and 60°C (with low RH) induced
757 significant compressive strength losses (Figure 3). This time, strength loss can probably be attributed
758 to carbonates and C-(A)-S-H reactions, possibly due to intercrystallite pores desaturation, dissolution-
759 precipitation, recrystallization or carbonation which may affect the porosity of the binder. This is
760 supported by changes in the structure of the hydrated products observed in GGBS-silicate dried at
761 60°C by Ismail et al. [10]. However, the results of our study do not allow us to conclude on a
762 mineralogical change due to drying (Figures 6; 7; 8). The kinetics of these reactions should be studied
763 in detail with the support of thermodynamic data. Since GGBS-silicate MIP porosity seemed to
764 increase for drying at 40°C (Table 4; Figure 4B) and SEM observations showed that the texture of the
765 gel was affected and looked like geopolymer paste dried at 60°C or 105°C (Figure 5), shrinkage and
766 micro/nano-cracking might occur, reducing mechanical strengths and creating voids.

767

768 Many authors have shown that, for a fixed temperature, relative humidity has a strong effect on the
769 material during drying [95]. Ye et al. [96] and Jia et al. [97] showed that the lower the relative
770 humidity and drying rate, the higher the shrinkage for alkali-activated slag materials, and so the
771 higher the chance of crack appearance. Drying at 40°C with a relative humidity of 80 % did not impact
772 the compressive strength of GGBS-silicate (Figure 3B). In Europe, a relative humidity of 50-65 % is

773 very common, but the temperature rarely stays at 40°C for long. In contrast, in arid deserts (e.g.
774 Sahara, Atacama, Namib), it is common to have 40°C with a very low RH. Inversely, in a humid
775 tropical environment it is common to have 40°C with a humidity close to 100 %. Depending on the
776 country, the temperature/relative humidity pair will vary and therefore play an important role during
777 drying, which can potentially affect the mortars differently.

778 Using Kelvin's law, it is possible to calculate the Kelvin radius (r_k) for mortar exposed at 40°C and both
779 20 and 80 %RH. According to Kelvin's law, with 40°C-20 %RH, the pores that are desaturated are
780 larger than 0.4 nm while, with 40°C-80 %RH it is only pores larger than 2.8 nm that are desaturated,
781 limiting the drying shrinkage. With a humidity rate of 80%, C-(A)-S-H intracrystallite pores were
782 desaturated ($0.6 \leq r \leq 1.6$ nm) while, with a humidity rate of 20% there were also intercrystallite
783 pores ($r \leq 0.6$ nm) [98,99]. It would therefore seem that the loss of mechanical resistance of a binder
784 is linked to the emptying of the intercrystallite C-(A)-S-H pores, inducing coarsening of pore structure,
785 probably attributable to the polymerization of silicate anion chains and the development of a
786 cohesive structure [100]. Some AAM are sensitive to moisture and may undergo a continuous
787 sequence of irreversible decomposition reactions during drying [11]. GGBS-silicate stored at 40°C
788 under autogenous conditions, or dried at 40°C – 80% RH, desaturated C-(A)-S-H intracrystallite pores
789 but not intercrystallite ones, which do not lead to a mechanical strength drop (Figure 3,
790 Supplementary data A). Nevertheless, this invites further investigation of the role of humidity and its
791 coupling with temperature.

792

793 One hypothesis to explain why the effect of desaturation at temperatures higher than 60°C did not
794 affect the compressive strength is that the kinetics of the drying is also of importance. At 60°C or
795 more, the material may be subjected to a shorter period of mechanical stress, limiting
796 microstructural damage. Ye et al. [96] and Hojati et al. [101] reported that their fine pore structure
797 and high degree of saturation found upon drying increased the effective capillary pressure, and slag
798 mixtures also showed a significant time dependent response (creep), where the pastes continued to

799 shrink after their maximum mass loss had been reached. Investigations by Ye and Radlińska [102]
800 and Ye et al. [103] have explained the high drying shrinkage of AAS by providing an understanding of
801 the behaviour of hydration products during the drying process. According to their research, the
802 structural incorporation of alkali cations in C-A-S-H reduces the stacking regularity of C-A-S-H layers
803 and facilitates their collapse and redistribution upon drying. The high drying shrinkage of AAS can be
804 attributed to the relatively low creep modulus of the hydration products in AAS.

805

806 **5.2.3. Mk-GGBS-silicate**

807

808 Intense micro-cracking was observed for mortar stored under autogenous conditions (Figure 5), and
809 was probably linked to a significant autogenous shrinkage favoured by the hydration of the slag.
810 Whatever the drying condition is, an increase in the pore size was observed (Figure 4), which could
811 be associated with nano-cracking and creation of porosity caused by drying shrinkage. As for the
812 geopolymer, the microstructure evolution could also be linked to the presence of quartz in the
813 metakaolin. As observed in another ternary mixture, a GGBS/fly ash geopolymer, the loss of water
814 related to drying is possibly related to the gel moving toward a less ordered and more cross-linked
815 structure [10]. Thus, both autogenous and drying shrinkage would probably be at the origin of the
816 drop in mechanical strength (Figure 9B), without there being any apparent mineralogical variation
817 (Figure 6).

818

819 Whatever the nature of the AAM, increasing the drying temperature (20°C to 125°C) induced no
820 mineralogical change but did lead to microstructural modifications due to autogenous and drying
821 shrinkage: disappearance of the smallest pores (< 10 nm) in favour of larger ones (10-100 nm, and
822 even 0.1-1 µm for geopolymer) that can be observed in SEM pictures and suggests the collapse of
823 fine pores with reorganization of the paste, and micro-cracking.

824

825 5.3. AAM drying recommendations

826

827 Experimental results in this manuscript refer to only four mixtures, without evaluation of their
828 robustness or the variability of raw materials. Starting with a different precursor or activator, in
829 terms of fineness, mineralogical or chemical composition, degree of crystallinity, etc., might lead to
830 significant differences in the experimental results. For example, the density and purity of metakaolin
831 governs its reactivity, as well as its autogenous deformation, which can be shrinkage or expansion
832 [104]. Likewise, the chemical composition of slag will determine its reactivity [105,106]. As shown in
833 numerous studies, activator dosage, water content and molar ratios will also influence the properties
834 of the alkali-activated material [94]. So, it should be kept in mind that the recommendations listed
835 below are valid for the raw materials and mixtures that we have tested, and should only be
836 generalized with caution.

837

838 Geopolymer (metakaolin rich in quartz activated with sodium silicate) showed a drop in mechanical
839 strength with oven drying at temperatures of 50°C to 125°C (Figure 3). This damage was correlated
840 with an increase in both MIP porosity and pore size (Table 4; Figure 4A) but, counterintuitively, fewer
841 large cracks were observed under SEM (Figure 5). It is likely that drying at over 50°C induced nano- to
842 micro-cracking, which damped the stresses generated by drying shrinkage and/or when the sample
843 was vacuumed in the SEM chamber, and thus prevented the formation of large fissures.

844 Oven drying at 40°C or less reduced the efficiency of drying, but retained mechanical properties (at
845 least 90% of strength of autogenous samples, Figure 9B). It did not seem to generate supplementary
846 micro-cracks, even though the pore size distribution began to be affected (Figures 4; 9D; 9E). No
847 mineralogical variation of the crystallized phases was observed between autogenous samples and
848 those dried at 40°C or 105°C (Figures 6; 7; 8). Oven drying at a temperature of 40°C appears to
849 provide a good compromise between quite efficient drying and little resulting damage, even if not all
850 free water is removed. This implies that standard methods requiring drying at 100-110°C should be

851 used with caution with metakaolin geopolymer (e.g. ASTM 642, 2006; Australian Standard AS1012,
852 1999; [107]). Finally, it seems that the only method found to preserve very small pores is freeze-
853 drying (Zhang et al. [12]; Supplementary data BS7). These findings are consistent with a study on OPC
854 by Konecny and Naqvi [108]. However, the method is not technically feasible with big samples, such
855 as on samples of 4x4x16 cm³ or bigger concrete samples.

856

857 GGBS-silicate and GGBS-carbonate mixtures have very different mineralogical compositions (Figure
858 7) but show globally similar behaviour during oven drying. For temperatures from 80°C to 125°C,
859 drying is fast and efficient (Figures 1; 2), strength properties do not appear to be affected (Figure 3)
860 and it seems that there are no new micro-cracks (Figure 5). In contrast, for both mixtures, oven
861 drying at 40°C to 60°C (at low relative humidity) induces a large compressive strength loss (Figure 3),
862 affects porosity (Table 4, Figures 4, 9), and generates micro-cracks (Figure 5). Compressive strength
863 loss was also observed on GGBS-carbonate concretes oven dried at 40°C [77]. Considering the
864 results, GGBS-based binder preconditioning should not include drying at 40-60°C but use a
865 temperature of at least 80°C to ensure quick drying. This is contrary to what is recommended in
866 some standard methods (e.g. ASTM C1585, 2011; EN 13057, 2002) or AAM studies [11]. As a
867 precautionary measure, it would be advisable to systematically assess the influence of
868 preconditioning by mechanical strength measurement before continuing with the durability tests.

869

870 Mk-GGBS-silicate was designed to combine the advantages of geopolymer and GGBS-silicate
871 systems. This seems to have been the case in view of the properties of the samples stored under
872 autogenous conditions. Unfortunately, during drying, Mk-GGBS-silicate mixture rather seems to
873 accumulate the disadvantages of both. Whatever the temperature used in the 20°C to 125°C range, a
874 significant drop in mechanical strength is observed after drying (Figure 3). This damage is correlated
875 with porosity and pore size increase (Table 4; Figures 4; 9), micro-crack formations (Figure 5) and
876 mineralogical variations (Figures 6; 7; 8). For this mixture, it is not possible to recommend a drying

877 temperature and other solutions may need to be considered, such as freeze drying, solvent
878 replacement drying [10,12,109] or supercritical drying [110,111]. However, these methods are more
879 costly and less practical. Vacuum drying is an often-used technique, tested here on geopolymer and
880 GGBS-silicate, but appears to be quite inefficient (Figure 1). Although the 50-50 metakaolin-slag
881 mixture results in an uninviting finding, requiring special precautions for durability tests, other
882 mixtures with one precursor more abundant than the other have shown much more encouraging
883 behaviour (not presented in this study) and deserve to be studied further.

884

885 **6. Conclusions**

886

887 Effects of drying with several temperatures from 20 to 125°C have been evaluated on four alkali-
888 activated mixture binders: a geopolymer (sodium silicate activated metakaolin), a sodium carbonate
889 activated GGBS, a sodium silicate activated GGBS and a sodium silicate activated mixture of 50 %
890 metakaolin with 50 % GGBS. Mixture robustness and variability of the raw materials were not
891 evaluated (as the influence of quartz in metakaolin), so the conclusions of this article cannot be
892 generalized to all alkali-activated binders without precautions being taken.

893

894 This study reveals that each mixture tested had different behaviour depending on the drying
895 temperature. The synthesis in Table 5 allows the optimal drying to be chosen according to the
896 characterization or durability test to be carried out.

897 For geopolymer, the microstructure is damaged for drying temperatures above 40°C but mineralogy
898 does not appear to be affected with our formula. This is linked to an increase in pore size and nano-
899 to microcracking, which is probably linked with shrinkage and a reorganization of the geopolymer
900 paste. For a test linked to the microstructure (e.g. strength, permeability, chloride migration,
901 carbonation) drying at 40°C will therefore be chosen, accepting that part of the water will still be

902 present in the porosity. On the other hand, for a test related to chemistry or mineralogy, a drying
903 temperature of 105°C will be a good option as it enables more water to be removed.

904 GGBS activated by silicate or carbonate should be dried at 105°C for most tests, with the exception of
905 those related to porosity, which require inefficient drying at 20°C. Note that drying at 40-60°C in a
906 low humidity environment considerably affects the mechanical strength. This is probably related to
907 desaturation of C-(A)-S-H intercrystallite pores in addition to drying shrinkage. The higher drying rate
908 at higher temperatures might limit the internal mechanical stress and preserve the material.

909 Finally, Mk-GGBS-silicate combines the drawbacks of geopolymer and GGBS-silicate and both
910 microstructure and mineralogical assemblage seem to be affected regardless of the drying
911 temperature used. However, by using other proportions between the two precursors, more
912 encouraging results can be obtained.

913

914 According to the data highlighted in this article, it is not possible to conclude on an optimal drying
915 temperature for all AAMs and all sustainability analyses. To ensure that the preconditioning step has
916 not been too harmful for a sample, it would be wise to always compare mechanical strength (or
917 ultrasonic pulse velocity for geopolymer) on dried and non-dried samples. If a significant difference is
918 observed between the two, it would then be necessary to distinguish the properties inherent in the
919 materials from those induced by preconditioning.

920

921 **7. References**

922

923 [1] J. Davidovits, Geopolymers: inorganic polymeric new materials, Journal of Thermal
924 Analysis and Calorimetry. 37 (1991) 1633–1656.

925 [2] J.L. Provis, J.S.J. van Deventer, Geopolymers: structures, processing, properties and
926 industrial applications, Elsevier, 2009.

- 927 [3] C. Shi, A.F. Jiménez, A. Palomo, New cements for the 21st century: The pursuit of an
928 alternative to Portland cement, *Cement and Concrete Research*. 41 (2011) 750–763.
929 <https://doi.org/10.1016/j.cemconres.2011.03.016>.
- 930 [4] F. Pacheco-Torgal, J.A. Labrincha, C. Leonelli, A. Palomo, P. Chindaprasirt, *Handbook*
931 *of Alkali-Activated Cements, Mortars and Concretes*, Elsevier, 2015.
932 <https://doi.org/10.1016/C2013-0-16511-7>.
- 933 [5] S.A. Bernal, J.L. Provis, Durability of alkali-activated materials: progress and
934 perspectives, *Journal of the American Ceramic Society*. 97 (2014) 997–1008.
- 935 [6] M.M. Hossain, M.R. Karim, M.K. Hossain, M.N. Islam, M.F.M. Zain, Durability of
936 mortar and concrete containing alkali-activated binder with pozzolans: A review,
937 *Construction and Building Materials*. 93 (2015) 95–109.
938 <https://doi.org/10.1016/j.conbuildmat.2015.05.094>.
- 939 [7] K. Arbi, M. Nedeljković, Y. Zuo, G. Ye, A Review on the Durability of Alkali-Activated
940 Fly Ash/Slag Systems: Advances, Issues, and Perspectives, *Ind. Eng. Chem. Res.* 55
941 (2016) 5439–5453. <https://doi.org/10.1021/acs.iecr.6b00559>.
- 942 [8] J. Zhang, C. Shi, Z. Zhang, Z. Ou, Durability of alkali-activated materials in aggressive
943 environments: A review on recent studies, *Construction and Building Materials*. 152
944 (2017) 598–613. <https://doi.org/10.1016/j.conbuildmat.2017.07.027>.
- 945 [9] T. Luukkonen, Z. Abdollahnejad, J. Yliniemi, P. Kinnunen, M. Illikainen, One-part alkali-
946 activated materials: A review, *Cement and Concrete Research*. 103 (2018) 21–34.
947 <https://doi.org/10.1016/j.cemconres.2017.10.001>.
- 948 [10] I. Ismail, S.A. Bernal, J.L. Provis, S. Hamdan, J.S.J. van Deventer, Drying-induced
949 changes in the structure of alkali-activated pastes, *J Mater Sci*. 48 (2013) 3566–3577.
950 <https://doi.org/10.1007/s10853-013-7152-9>.

- 951 [11] K. Yang, C. Yang, B. Magee, S. Nanukuttan, J. Ye, Establishment of a
952 preconditioning regime for air permeability and sorptivity of alkali-activated slag
953 concrete, *Cement and Concrete Composites*. 73 (2016) 19–28.
954 <https://doi.org/10.1016/j.cemconcomp.2016.06.019>.
- 955 [12] Z. Zhang, Y. Zhu, H. Zhu, Y. Zhang, J.L. Provis, H. Wang, Effect of drying
956 procedures on pore structure and phase evolution of alkali-activated cements, *Cement and*
957 *Concrete Composites*. 96 (2019) 194–203.
958 <https://doi.org/10.1016/j.cemconcomp.2018.12.003>.
- 959 [13] G.J. Gluth, K. Arbi, S.A. Bernal, D. Bondar, A. Castel, S. Chithiraputhiran, A.
960 Dehghan, K. Dombrowski-Daube, A. Dubey, V. Ducman, RILEM TC 247-DTA round
961 robin test: carbonation and chloride penetration testing of alkali-activated concretes,
962 *Materials and Structures*. 53 (2020) 1–17.
- 963 [14] F. Winnefeld, G.J. Gluth, S.A. Bernal, M.C. Bignozzi, L. Carabba, S.
964 Chithiraputhiran, A. Dehghan, S. Dolenc, K. Dombrowski-Daube, A. Dubey, RILEM
965 TC 247-DTA round robin test: sulfate resistance, alkali-silica reaction and freeze–thaw
966 resistance of alkali-activated concretes, *Materials and Structures*. 53 (2020) 1–17.
- 967 [15] S.A. Bernal, R. San Nicolas, J.L. Provis, R. Mejía de Gutiérrez, J.S.J. van Deventer,
968 Natural carbonation of aged alkali-activated slag concretes, *Mater Struct*. 47 (2014) 693–
969 707. <https://doi.org/10.1617/s11527-013-0089-2>.
- 970 [16] J.L. Provis, J.S. Van Deventer, eds., *Alkali activated materials: State-of-the-art Report*,
971 *Rilem Tc 224-AAM*, Springer, Dordrecht, 2014.
- 972 [17] M. Kovtun, Effect of Preconditioning on Durability Indices of Alkali-Activated
973 Concretes, *SP*. 326 (2018) 19.1-19.6.
- 974 [18] N.C. Collier, J.H. Sharp, N.B. Milestone, J. Hill, I.H. Godfrey, The influence of water
975 removal techniques on the composition and microstructure of hardened cement pastes,

- 976 Cement and Concrete Research. 38 (2008) 737–744.
977 <https://doi.org/10.1016/j.cemconres.2008.02.012>.
- 978 [19] A. Bogner, J. Schatz, F. Dehn, H.S. Müller, Influence of Drying on the Microstructure
979 of Hardened Cement Paste: A Mercury Intrusion Porosimetry, Nitrogen Sorption and
980 SAXS Study, ACT. 18 (2020) 83–94. <https://doi.org/10.3151/jact.18.83>.
- 981 [20] C. Gallé, Effect of drying on cement-based materials pore structure as identified by
982 mercury intrusion porosimetry A comparative study between oven-, vacuum-, and freeze-
983 drying, Cement and Concrete Research. (2001) 11.
- 984 [21] J.J. Beaudoin, A discussion on, “The use of nitrogen adsorption to assess the
985 microstructure of cement paste” by M.C.G. Juenger and H.M. Jennings, Cement and
986 Concrete Research. 32 (2002) 831–832. [https://doi.org/10.1016/S0008-8846\(01\)00742-6](https://doi.org/10.1016/S0008-8846(01)00742-6).
- 987 [22] J. Zhang, G.W. Scherer, Comparison of methods for arresting hydration of cement,
988 Cement and Concrete Research. 41 (2011) 1024–1036.
989 <https://doi.org/10.1016/j.cemconres.2011.06.003>.
- 990 [23] K.K. Aligizaki, Pore structure of cement-based materials: testing, interpretation and
991 requirements, Taylor & Francis, Abingdon [England] ; New York, 2006.
- 992 [24] A. Korpa, R. Trettin, The influence of different drying methods on cement paste
993 microstructures as reflected by gas adsorption: Comparison between freeze-drying (F-
994 drying), D-drying, P-drying and oven-drying methods, Cement and Concrete Research. 36
995 (2006) 634–649. <https://doi.org/10.1016/j.cemconres.2005.11.021>.
- 996 [25] D. Snoeck, L.F. Velasco, A. Mignon, S. Van Vlierberghe, P. Dubruel, P. Lodewyckx,
997 N. De Belie, The influence of different drying techniques on the water sorption properties
998 of cement-based materials, Cement and Concrete Research. 64 (2014) 54–62.
999 <https://doi.org/10.1016/j.cemconres.2014.06.009>.

- 1000 [26] R. Snellings, J. Chwast, Ö. Cizer, N. De Belie, Y. Dhandapani, P. Durdzinski, J. Elsen,
1001 J. Haufe, D. Hooton, C. Patapy, M. Santhanam, K. Scrivener, D. Snoeck, L. Steger, S.
1002 Tongbo, A. Vollpracht, F. Winnefeld, B. Lothenbach, Report of TC 238-SCM: hydration
1003 stoppage methods for phase assemblage studies of blended cements—results of a round
1004 robin test, *Mater Struct.* 51 (2018) 111. <https://doi.org/10.1617/s11527-018-1237-5>.
- 1005 [27] Z. Zhang, G.W. Scherer, Evaluation of drying methods by nitrogen adsorption,
1006 *Cement and Concrete Research.* 120 (2019) 13–26.
1007 <https://doi.org/10.1016/j.cemconres.2019.02.016>.
- 1008 [28] C. Rößler, A. Eberhardt, H. Kučerová, B. Möser, Influence of hydration on the fluidity
1009 of normal Portland cement pastes, *Cement and Concrete Research.* 38 (2008) 897–906.
1010 <https://doi.org/10.1016/j.cemconres.2008.03.003>.
- 1011 [29] J.J. Beaudoin, P. Gu, J. Marchand, B. Tamtsia, R.E. Myers, Z. Liu, Solvent
1012 Replacement Studies of Hydrated Portland Cement Systems: The Role of Calcium
1013 Hydroxide, *Advanced Cement Based Materials.* 8 (1998) 56–65.
1014 [https://doi.org/10.1016/S1065-7355\(98\)00008-X](https://doi.org/10.1016/S1065-7355(98)00008-X).
- 1015 [30] L. Zhang, F.P. Glasser, Critical examination of drying damage to cement pastes,
1016 *Advances in Cement Research.* 12 (2000) 79–88.
1017 <https://doi.org/10.1680/adcr.2000.12.2.79>.
- 1018 [31] M. Giroudon, M. Peyre Lavigne, C. Patapy, A. Bertron, Blast-furnace slag cement and
1019 metakaolin based geopolymer as construction materials for liquid anaerobic digestion
1020 structures: Interactions and biodeterioration mechanisms, *Science of The Total
1021 Environment.* 750 (2021) 141518. <https://doi.org/10.1016/j.scitotenv.2020.141518>.
- 1022 [32] R. San Nicolas, M. Cyr, G. Escadeillas, Characteristics and applications of flash
1023 metakaolins, *Applied Clay Science.* 83–84 (2013) 253–262.
1024 <https://doi.org/10.1016/j.clay.2013.08.036>.

- 1025 [33] R. Pouhet, M. Cyr, Formulation and performance of flash metakaolin geopolymer
1026 concretes, *Construction and Building Materials*. 120 (2016) 150–160.
1027 <https://doi.org/10.1016/j.conbuildmat.2016.05.061>.
- 1028 [34] R. Pouhet, M. Cyr, R. Bucher, Influence of the initial water content in flash calcined
1029 metakaolin-based geopolymer, *Construction and Building Materials*. 201 (2019) 421–429.
1030 <https://doi.org/10.1016/j.conbuildmat.2018.12.201>.
- 1031 [35] H. Lahalle, V. Benavent, V. Trincal, T. Wattez, R. Bucher, M. Cyr, Robustness to
1032 water and temperature, and activation energies of metakaolin-based geopolymer and
1033 alkali-activated slag binders, *Construction and Building Materials*. 300 (2021) 124066.
1034 <https://doi.org/10.1016/j.conbuildmat.2021.124066>.
- 1035 [36] H.C. Hardy, D. Telfair, W.H. Pielemeier, The Velocity of Sound in Air, *The Journal*
1036 *of the Acoustical Society of America*. 13 (1942) 9. [https://doi.org/doi:](https://doi.org/doi:10.1121/1.1916169)
1037 [10.1121/1.1916169](https://doi.org/doi:10.1121/1.1916169).
- 1038 [37] S.W. Kieffer, Sound speed in liquid-gas mixtures: Water-air and water-steam, *J.*
1039 *Geophys. Res.* 82 (1977) 2895–2904. <https://doi.org/10.1029/JB082i020p02895>.
- 1040 [38] A. Quiviger, Ultrasons diffus pour la caractérisation d'une fissure dans le béton.:
1041 approche linéaire et non linéaire., PhD Thesis, Aix-Marseille, 2012.
- 1042 [39] M.G. Hernández, M.A.G. Izquierdo, A. Ibáñez, J.J. Anaya, L.G. Ullate, Porosity
1043 estimation of concrete by ultrasonic NDE, *Ultrasonics*. 38 (2000) 531–533.
1044 [https://doi.org/10.1016/S0041-624X\(99\)00095-5](https://doi.org/10.1016/S0041-624X(99)00095-5).
- 1045 [40] Z. Lafhaj, M. Goueygou, A. Djerbi, M. Kaczmarek, Correlation between porosity,
1046 permeability and ultrasonic parameters of mortar with variable water/cement ratio and
1047 water content, *Cement and Concrete Research*. 36 (2006) 625–633.
1048 <https://doi.org/10.1016/j.cemconres.2005.11.009>.

- 1049 [41] N. Toubal Seghir, O. Benaimeche, K. Krzywiński, Ł. Sadowski, Ultrasonic Evaluation
1050 of Cement-Based Building Materials Modified Using Marble Powder Sourced from
1051 Industrial Wastes, *Buildings*. 10 (2020) 38. <https://doi.org/10.3390/buildings10030038>.
- 1052 [42] J. Zhu, S.-H. Kee, D. Han, Y.-T. Tsai, Effects of air voids on ultrasonic wave
1053 propagation in early age cement pastes, *Cement and Concrete Research*. 41 (2011) 872–
1054 881. <https://doi.org/10.1016/j.cemconres.2011.04.005>.
- 1055 [43] E. Ohdaira, N. Masuzawa, Water content and its effect on ultrasound propagation in
1056 concrete — the possibility of NDE, *Ultrasonics*. 38 (2000) 546–552.
1057 [https://doi.org/10.1016/S0041-624X\(99\)00158-4](https://doi.org/10.1016/S0041-624X(99)00158-4).
- 1058 [44] T.P. Philippidis, D.G. Aggelis, Experimental study of wave dispersion and attenuation
1059 in concrete, *Ultrasonics*. 43 (2005) 584–595. <https://doi.org/10.1016/j.ultras.2004.12.001>.
- 1060 [45] W. Wang, C. Lu, G. Yuan, Y. Zhang, Effects of pore water saturation on the
1061 mechanical properties of fly ash concrete, *Construction and Building Materials*. 130
1062 (2017) 54–63. <https://doi.org/10.1016/j.conbuildmat.2016.11.031>.
- 1063 [46] Ma.D.E. Candelaria, S.-H. Kee, J.-J. Yee, J.-W. Lee, Effects of Saturation Levels on
1064 the Ultrasonic Pulse Velocities and Mechanical Properties of Concrete, *Materials*. 14
1065 (2021) 152. <https://doi.org/10.3390/ma14010152>.
- 1066 [47] F. Saint-Pierre, A. Philibert, B. Giroux, P. Rivard, Concrete Quality Designation based
1067 on Ultrasonic Pulse Velocity, *Construction and Building Materials*. 125 (2016) 1022–
1068 1027. <https://doi.org/10.1016/j.conbuildmat.2016.08.158>.
- 1069 [48] S. Hong, S. Yoon, J. Kim, C. Lee, S. Kim, Y. Lee, Evaluation of Condition of
1070 Concrete Structures Using Ultrasonic Pulse Velocity Method, *Applied Sciences*. 10
1071 (2020) 19.

- 1072 [49] S. Ould Naffa, M. Goueygou, B. Piwakowski, F. Buyle-Bodin, Detection of chemical
1073 damage in concrete using ultrasound, *Ultrasonics*. 40 (2002) 247–251.
1074 [https://doi.org/10.1016/S0041-624X\(02\)00146-4](https://doi.org/10.1016/S0041-624X(02)00146-4).
- 1075 [50] F. Saint-Pierre, P. Rivard, G. Ballivy, Measurement of alkali–silica reaction
1076 progression by ultrasonic waves attenuation, *Cement and Concrete Research*. 37 (2007)
1077 948–956. <https://doi.org/10.1016/j.cemconres.2007.02.022>.
- 1078 [51] D.A. Bohn, Environmental effects on the speed of sound, in: *Audio Engineering*
1079 *Society Convention 83*, Audio Engineering Society, 1987.
- 1080 [52] G. Ye, P. Lura, K. van Breugel, A.L.A. Fraaij, Study on the development of the
1081 microstructure in cement-based materials by means of numerical simulation and
1082 ultrasonic pulse velocity measurement, *Cement and Concrete Composites*. 26 (2004) 491–
1083 497. [https://doi.org/10.1016/S0958-9465\(03\)00081-7](https://doi.org/10.1016/S0958-9465(03)00081-7).
- 1084 [53] J. Berriman, P. Purnell, D.A. Hutchins, A. Neild, Humidity and aggregate content
1085 correction factors for air-coupled ultrasonic evaluation of concrete, *Ultrasonics*. 43 (2005)
1086 211–217. <https://doi.org/10.1016/j.ultras.2004.07.003>.
- 1087 [54] W. López, J.A. González, Influence of the degree of pore saturation on the resistivity
1088 of concrete and the corrosion rate of steel reinforcement, *Cement and Concrete Research*.
1089 23 (1993) 368–376. [https://doi.org/10.1016/0008-8846\(93\)90102-F](https://doi.org/10.1016/0008-8846(93)90102-F).
- 1090 [55] P. Rivard, F. Saint-Pierre, Assessing alkali-silica reaction damage to concrete with
1091 non-destructive methods: From the lab to the field, *Construction and Building Materials*.
1092 23 (2009) 902–909. <https://doi.org/10.1016/j.conbuildmat.2008.04.013>.
- 1093 [56] P.J. Tumidajski, A.S. Schumacher, S. Perron, P. Gu, J.J. Beaudoin, On the relationship
1094 between porosity and electrical resistivity in cementitious systems, *Cement and Concrete*
1095 *Research*. 26 (1996) 539–544. [https://doi.org/10.1016/0008-8846\(96\)00017-8](https://doi.org/10.1016/0008-8846(96)00017-8).
- 1096 [57] E.W. Washburn, The dynamics of capillary flow, *Physical Review*. 17 (1921) 273.

- 1097 [58] Micromeritics, AutoPore IV 9500 - Operator's Manual Rev A - 950-42801-01, 2015.
- 1098 [59] M. Gasc-Barbier, S. Chanchole, De l'utilisation d'échantillons humides en
1099 porosimétrie au mercure, *Revue Française de Géotechnique*. (2005) 7.
- 1100 [60] M. Staněk, Y. Géraud, Granite microporosity changes due to fracturing and alteration:
1101 secondary mineral phases as proxies for porosity and permeability estimation, *Solid Earth*.
1102 10 (2019) 251–274. <https://doi.org/10.5194/se-10-251-2019>.
- 1103 [61] J.M. Ortega, M. Cabeza, A.J. Tenza-Abril, T. Real-Herraiz, M.Á. Climent, I. Sánchez,
1104 Effects of red mud addition in the microstructure, durability and mechanical performance
1105 of cement mortars, *Applied Sciences*. 9 (2019) 984.
- 1106 [62] M. Thiery, Modelling of atmospheric carbonation of cement based materials
1107 considering the kinetic effects and modifications of the microstructure and the hydric
1108 state, PhD Thesis, Ecole des Ponts ParisTech, 2005.
- 1109 [63] S. Stephant, Étude de l'influence de l'hydratation des laitiers sur les propriétés de
1110 transfert gazeux dans les matériaux cimentaires, PhD Thesis, Université de Bourgogne,
1111 2015. <http://rgdoi.net/10.13140/RG.2.1.1665.4483>.
- 1112 [64] R.L. Portsmouth, L.F. Gladden, Determination of pore connectivity by mercury
1113 porosimetry, *Chemical Engineering Science*. 46 (1991) 3023–3036.
1114 [https://doi.org/10.1016/0009-2509\(91\)85006-J](https://doi.org/10.1016/0009-2509(91)85006-J).
- 1115 [65] V.G. Mata, J.C.B. Lopes, M.M. Dias, Porous media characterization using mercury
1116 porosimetry simulation. 1. Description of the simulator and its sensitivity to model
1117 parameters, *Industrial & Engineering Chemistry Research*. 40 (2001) 3511–3522.
- 1118 [66] V.G. Mata, J.C.B. Lopes, M.M. Dias, Porous media characterization using mercury
1119 porosimetry simulation. 2. An iterative method for the determination of the real pore size
1120 distribution and the mean coordination number, *Industrial & Engineering Chemistry
1121 Research*. 40 (2001) 4836–4843.

- 1122 [67] V. Trinca, D. Charpentier, M.D. Buatier, B. Grobety, B. Lacroix, P. Labaume, J.-P.
1123 Sizun, Quantification of mass transfers and mineralogical transformations in a thrust fault
1124 (Monte Perdido thrust unit, southern Pyrenees, Spain), *Marine and Petroleum Geology*. 55
1125 (2014) 160–175. <https://doi.org/10.1016/j.marpetgeo.2013.12.016>.
- 1126 [68] J.L. Kulp, P. Kent, P.F. Kerr, Thermal study of the Ca-Mg-Fe carbonate minerals,
1127 *American Mineralogist*. 36 (1951) 643–670.
- 1128 [69] M. Földvári, Handbook of thermogravimetric system of minerals and its use in
1129 geological practice, 2011. [https://geo-](https://geo-portal.hu/sites/default/files/files/K%C3%B6nyvtar/Alkalmi_teljes/Fodvari_egyben.pdf)
1130 [portal.hu/sites/default/files/files/K%C3%B6nyvtar/Alkalmi_teljes/Fodvari_egyben.pdf](https://geo-portal.hu/sites/default/files/files/K%C3%B6nyvtar/Alkalmi_teljes/Fodvari_egyben.pdf).
- 1131 [70] W. Thomson, On the Equilibrium of Vapour at a Curved Surface of Liquid, *Proc. R.*
1132 *Soc. Edinb.* 7 (1872) 63–68. <https://doi.org/10.1017/S0370164600041729>.
- 1133 [71] H. Ye, A. Radlińska, A review and comparative study of existing shrinkage prediction
1134 models for portland and non-portland cementitious materials, *Advances in Materials*
1135 *Science and Engineering*. 2016 (2016).
- 1136 [72] V. Benavent, Caractérisation de la porosité des géopolymères: évolution temporelle et
1137 étude de l'eau confinée, PhD Thesis, Montpellier, 2016.
- 1138 [73] P. Duxson, G.C. Lukey, J.S. van Deventer, Physical evolution of Na-geopolymer
1139 derived from metakaolin up to 1000 C, *Journal of Materials Science*. 42 (2007) 3044–
1140 3054.
- 1141 [74] J. Rouyer, V. Benavent, F. Frizon, A. Poulesquen, Influence of geopolymer
1142 formulation parameters on the elastic and porous properties over a one-year monitoring,
1143 *Materials Letters*. 207 (2017) 121–124. <https://doi.org/10.1016/j.matlet.2017.06.125>.
- 1144 [75] S.J. Barnett, M.N. Soutsos, S.G. Millard, J.H. Bungey, Strength development of
1145 mortars containing ground granulated blast-furnace slag: Effect of curing temperature and

1146 determination of apparent activation energies, *Cement and Concrete Research*. 36 (2006)
1147 434–440. <https://doi.org/10.1016/j.cemconres.2005.11.002>.

1148 [76] F. Sajedi, H.A. Razak, Comparison of different methods for activation of ordinary
1149 Portland cement-slag mortars, *Construction and Building Materials*. 25 (2011) 30–38.
1150 <https://doi.org/10.1016/j.conbuildmat.2010.06.060>.

1151 [77] P. Azar, G. Samson, F. Deby, H. Lahalle, V. Benavent, M. Cyr, Chloride-induced
1152 corrosion in ordinary and alkali-activated concrete, (2020) 20.

1153 [78] S. Diamond, A discussion of the paper “Effect of drying on cement-based materials
1154 pore structure as identified by mercury porosimetry—a comparative study between oven-,
1155 vacuum-, and freeze-drying” by C. Gallé, *Cement and Concrete Research*. 33 (2003) 169–
1156 170. [https://doi.org/10.1016/S0008-8846\(02\)00940-7](https://doi.org/10.1016/S0008-8846(02)00940-7).

1157 [79] V. Benavent, F. Frizon, A. Poulesquen, Effect of composition and aging on the porous
1158 structure of metakaolin-based geopolymers, *Journal of Applied Crystallography*. 49
1159 (2016) 2116–2128. <https://doi.org/10.1107/S1600576716014618>.

1160 [80] V. Thiéry, V. Trincal, C.A. Davy, The elusive ettringite under the high-vacuum SEM
1161 – a reflection based on natural samples, the use of Monte Carlo modelling of EDS
1162 analyses and an extension to the ettringite group minerals, *Journal of Microscopy*. (2017)
1163 n/a-n/a. <https://doi.org/10.1111/jmi.12589>.

1164 [81] K.O. Kjellsen, H.M. Jennings, Observations of microcracking in cement paste upon
1165 drying and rewetting by environmental scanning electron microscopy, *Advanced Cement
1166 Based Materials*. 3 (1996) 14–19.

1167 [82] S.A. Bernal, J.L. Provis, V. Rose, R.M. De Gutierrez, Evolution of binder structure in
1168 sodium silicate-activated slag-metakaolin blends, *Cement and Concrete Composites*. 33
1169 (2011) 46–54.

- 1170 [83] M. Criado, A. Palomo, A. Fernandezjimenez, Alkali activation of fly ashes. Part 1:
1171 Effect of curing conditions on the carbonation of the reaction products, *Fuel*. 84 (2005)
1172 2048–2054. <https://doi.org/10.1016/j.fuel.2005.03.030>.
- 1173 [84] X. Guo, H. Shi, Metakaolin-, fly ash-and calcium hydroxide-based geopolymers:
1174 effects of calcium on performance, *Advances in Cement Research*. 27 (2015) 559–566.
- 1175 [85] M. Król, J. Minkiewicz, W. Mozgawa, IR spectroscopy studies of zeolites in
1176 geopolymeric materials derived from kaolinite, *Journal of Molecular Structure*. 1126
1177 (2016) 200–206.
- 1178 [86] M.A. Villaquirán-Caicedo, R.M. de Gutiérrez, S. Sulekar, C. Davis, J.C. Nino,
1179 Thermal properties of novel binary geopolymers based on metakaolin and alternative
1180 silica sources, *Applied Clay Science*. 118 (2015) 276–282.
- 1181 [87] M.R. Rowles, J.V. Hanna, K.J. Pike, M.E. Smith, B.H. O’Connor, ²⁹Si, ²⁷Al, ¹H and
1182 ²³Na MAS NMR Study of the Bonding Character in Aluminosilicate Inorganic Polymers,
1183 *Appl Magn Reson*. 32 (2007) 663–689. <https://doi.org/10.1007/s00723-007-0043-y>.
- 1184 [88] Q.H. Nguyen, M. Hanafi, J. Merkl, J.-B. d’Espinoise de Lacaille, Evolution of the
1185 microstructure of unconsolidated geopolymers by thermoporometry, *Journal of the*
1186 *American Ceramic Society*. 104 (2021) 1581–1591.
- 1187 [89] M.J. DeJong, F.-J. Ulm, The nanogranular behavior of CSH at elevated temperatures
1188 (up to 700 C), *Cement and Concrete Research*. 37 (2007) 1–12.
- 1189 [90] E.T. Rodriguez, K. Garbey, D. Merz, L. Black, I.G. Richardson, Thermal stability of
1190 CSH phases and applicability of Richardson and Groves’ and Richardson C-(A)-SH (I)
1191 models to synthetic CSH, *Cement and Concrete Research*. 93 (2017) 45–56.
- 1192 [91] Y. He, X. Zheng, L. Lü, S. Yu, G. Deng, S. Hu, Dehydration Characteristics of CSH
1193 with Ca/Si Ratio 1.0 Prepared Via Precipitation, *Journal of Wuhan University of*
1194 *Technology-Mater. Sci. Ed*. 33 (2018) 619–624.

- 1195 [92] A. Abdalqader, F. Jin, A. Al-Tabbaa, Performance of magnesia-modified sodium
1196 carbonate-activated slag/fly ash concrete, *Cement and Concrete Composites*. 103 (2019)
1197 160–174.
- 1198 [93] R.R. Lloyd, The durability of inorganic polymer cements, PhD Thesis, 2008.
- 1199 [94] C. Kuenzel, L.J. Vandeperre, S. Donatello, A.R. Boccaccini, C. Cheeseman, Ambient
1200 temperature drying shrinkage and cracking in metakaolin-based geopolymers, *Journal of*
1201 *the American Ceramic Society*. 95 (2012) 3270–3277.
- 1202 [95] P. Gao, Effect of relative humidity on drying-induced damage in concrete: A
1203 comparative study of digital image correlation and lattice modelling, *Materials and*
1204 *Design*. (2020) 17.
- 1205 [96] H. Ye, C. Cartwright, F. Rajabipour, A. Radlińska, Effect of drying rate on shrinkage
1206 of alkali-activated slag cements, (2014).
- 1207 [97] Z. Jia, Y. Yang, L. Yang, Y. Zhang, Z. Sun, Hydration products, internal relative
1208 humidity and drying shrinkage of alkali activated slag mortar with expansion agents,
1209 *Construction and Building Materials*. 158 (2018) 198–207.
1210 <https://doi.org/10.1016/j.conbuildmat.2017.09.162>.
- 1211 [98] M. Daimon, S.A. Abo-El-Enein, G. Hosaka, S. Goto, Pore Structure of Calcium
1212 Silicate Hydrate in Hydrated Tricalcium Silicate, 60 (1977) 5.
- 1213 [99] A. Plassais, Nanoporosité, texture et propriétés mécaniques de pâtes de ciments, PhD
1214 Thesis, Université Pierre et Marie Curie, 2003.
- 1215 [100] Y. Aono, F. Matsushita, S. Shibata, Y. Hama, Nano-structural Changes of C-S-H in
1216 Hardened Cement Paste during Drying at 50°C, *ACT*. 5 (2007) 313–323.
1217 <https://doi.org/10.3151/jact.5.313>.

- 1218 [101] M. Hojati, F. Rajabipour, A. Radlińska, Drying shrinkage of alkali-activated cements:
1219 effect of humidity and curing temperature, *Mater Struct.* 52 (2019) 118.
1220 <https://doi.org/10.1617/s11527-019-1430-1>.
- 1221 [102] H. Ye, A. Radlińska, Shrinkage mechanisms of alkali-activated slag, *Cement and*
1222 *Concrete Research.* 88 (2016) 126–135.
- 1223 [103] H. Ye, C. Cartwright, F. Rajabipour, A. Radlińska, Understanding the drying
1224 shrinkage performance of alkali-activated slag mortars, *Cement and Concrete*
1225 *Composites.* 76 (2017) 13–24. <https://doi.org/10.1016/j.cemconcomp.2016.11.010>.
- 1226 [104] Z. Li, G. Ye, Experimental study of the chemical deformation of metakaolin based
1227 geopolymer, *Proceedings of the SynerCrete.* 18 (2018).
- 1228 [105] S. Blotevogel, A. Ehrenberg, L. Steger, L. Doussang, J. Kaknics, C. Patapy, M. Cyr,
1229 Ability of the R3 test to evaluate differences in early age reactivity of 16 industrial ground
1230 granulated blast furnace slags (GGBS), *Cement and Concrete Research.* 130 (2020)
1231 105998.
- 1232 [106] S. Blotevogel, L. Steger, D. Hart, L. Doussang, J. Kaknics, M. Poirier, H. Bornhöft, J.
1233 Deubener, C. Patapy, M. Cyr, Effect of TiO₂ and 11 minor elements on the reactivity of
1234 ground-granulated blast-furnace slag in blended cements, *Journal of the American*
1235 *Ceramic Society.* 104 (2021) 128–139.
- 1236 [107] T.C. Rilem, 116-PCD. Permeability of concrete as a criterion of its durability,
1237 *Materials and Structures.* 32 (1999) 174–179.
- 1238 [108] L. Konecny, S.J. Naqvi, The effect of different drying techniques on the pore size
1239 distribution of blended cement mortars, *Cement and Concrete Research.* 23 (1993) 1223–
1240 1228. [https://doi.org/10.1016/0008-8846\(93\)90183-A](https://doi.org/10.1016/0008-8846(93)90183-A).

1241 [109] L.D. Mitchell, J.C. Margeson, The effects of solvents on C–S–H as determined by
1242 thermal analysis, *J Therm Anal Calorim.* 86 (2006) 591–594.
1243 <https://doi.org/10.1007/s10973-006-7712-1>.

1244 [110] Z. Zhang, G.W. Scherer, Supercritical drying of cementitious materials, *Cement and*
1245 *Concrete Research.* 99 (2017) 137–154. <https://doi.org/10.1016/j.cemconres.2017.05.005>.

1246 [111] G.W. Scherer, Stress and strain during supercritical drying, *J Sol-Gel Sci Technol.* 90
1247 (2019) 8–19. <https://doi.org/10.1007/s10971-018-4808-6>.

1248

1249

1250

1251 AFPC–AFREM (1997) Détermination de la masse volumique apparente et de la porosité accessible à
1252 l’eau, Méthodes recommandées pour la mesure des grandeurs associées à la durabilité. In
1253 *Compte-rendu des Journées Techniques* pp. 121–124. Toulouse.

1254 AS 1012 (1999) *Methods of Testing Concrete Method 21: Determination of water absorption and*
1255 *apparent volume of permeable voids in hardened concrete.*

1256 ASTM C642 (2006) *Standard test method for density, absorption, and voids in hardened concrete.*

1257 ASTM C1585 (2011) *Standard test method for measurement of rate of absorption of water by*
1258 *hydraulic cement concretes.*

1259 ISO 15901-1 (2005) *Evaluation of pore size distribution and porosimetry of solid materials by mercury*
1260 *porosimetry and gas adsorption – Part1: Mercury porosimetry.* 26p.

1261 ISO 1920-7 (2004) *Testing of concrete - Part 7: Non-destructive tests on hardened concrete.* 11p.

1262 NF EN 196-1 (2016) *Methods of testing cement – Part 1 : Determination of strength.* P15-471-1. 38p.

1263 NF EN 197-1 (2012) *Cement - Part 1: Composition, spécifications et critères de conformité des ciments*
1264 *courants. Specifications and Conformity Criteria for Common Cements.*

1265 NF EN 12390-2 (2019) *Testing hardened concrete - Part 2: Making and curing specimens for strength*
1266 *tests.* AFNOR 9p.

- 1267 NF EN 12504-4 (2005) Testing concrete – Part 4: Determination of ultrasonic pulse velocity. P18-447.
1268 17p.
- 1269 NF EN 13057 (2002) Products and systems for the protection and repair of concrete structures – Test
1270 methods – Determination of resistance of capillary absorption. P18-945. 13p.
- 1271 NF P 18-459 (2010) Concrete – Testing hardened concrete – Testing porosity and density. P18-459. 9p.
- 1272 SIA 262/1 (2013) Concrete Structures – Supplementary specifications p. 52. Société suisse des
1273 ingénieurs.
- 1274 XP P 18-458 (2008) Tests for hardened concrete – Accelerated carbonation test – Measurement of the
1275 thickness of carbonated concrete. P18-458. 12p.
- 1276 XP P 18-463 (2011) Concrete – Testing gas permeability on hardened concrete. P18-463. 7p.

1277

1278 **Acknowledgments**

1279

1280 The authors would like to thank Marc Begue, engineer at INSA Toulouse, who helped set up the
1281 porosimetry tests and Guillaume Lambare, assistant engineer at UPS Toulouse, for his contribution to
1282 TGA analyses. Thanks also to the technician Rémi Pradier, who actively contributed to the project for
1283 6 months. This work is part of the L2A chair (alkali-activated binders) grouping industrial partners
1284 EDF, VINCI Construction, ECOCEM Group, ARGECO Développement, VICAT and MBCC Group with the
1285 LMDC research laboratory.

1286

1287 **Figure captions**

1288

1289 **Figure 1:** Mortar mass monitoring during drying at different temperatures of the geopolymer (a),
1290 GGBS-silicate (b), GGBS-carbonate (c), Mk-GGBS-silicate (d), CEM I (e) and CEM III/B (f). For each
1291 temperature, data from at least four AAM specimens are superimposed on the figure, while there

1292 are only two samples for Portland cement-based binders. Large dots correspond to the end of drying
1293 (including an additional safety margin of one week) and therefore the age used for the
1294 physicochemical analyses.

1295

1296 **Figure 2:** Water content V_w (wt%) of mortars at the end of drying, obtained by subtracting the mass
1297 change due to conditioning (assumed to be water only) from the mixing water.

1298

1299 **Figure 3:** Compressive strengths (f_c) of mortars cured in autogenous conditions (black spots) or dried
1300 at different temperatures (after autogenous treatment of 28 days). Geopolymer (a), GGBS-silicate
1301 (b), GGBS-carbonate (c), Mk-GGBS-silicate (d), CEM I (e) and CEM III/B (f). Each point corresponds to
1302 the average of three analyses carried out on a $4 \times 4 \times 16 \text{ cm}^3$ sample and given in Supplementary data
1303 A.

1304

1305 **Figure 4:** Mortars pore size distribution for autogenous and dried of geopolymer (a-b), GGBS-silicate
1306 (c-d), GGBS-carbonate (e-f) and Mk-GGBS-silicate (g-h). Autogenous column in dried conditions
1307 graphs represents the average of the samples stored under autogenous conditions and analysed at
1308 different ages (28 to 88 days).

1309

1310 **Figure 5:** SEM backscattered observation of autogenous and dried AAM. Geopolymer dried for 14
1311 days at 40°C (a) or at 105°C (b); GGBS-silicate cured 88 days in autogenous conditions (c) or dried for
1312 35 days at 40°C (d); GGBS-carbonate dried for 35 days at 40°C (e) or 14 days at 105°C (f); Mk-GGBS-
1313 silicate cured for 88 days in autogenous conditions (g) or dried for 24 days at 60°C . More SEM
1314 pictures are given in Supplementary data BS6.

1315

1316 **Figure 6:** X-ray diffractograms obtained on crushed pastes of geopolymer (A), GGBS-silicate (B),
1317 GGBS-carbonate (C) and Mk-GGBS-silicate (D).

1318

1319 **Figure 7:** Representative FTIR normalized spectra obtained on crushed pastes of geopolymer (a),
1320 GGBS-silicate (b), GGBS-carbonate (c) and Mk-GGBS-silicate (d) cured at 20°C in autogenous
1321 conditions then dried at different temperatures.

1322

1323 **Figure 8:** Thermogravimetric analyses measured from room temperature to 1050°C performed on
1324 crushed pastes of geopolymer (a), GGBS-silicate (b), GGBS-carbonate (c) and Mk-GGBS-silicate (d).

1325

1326 **Figure 9:** Drying impact versus temperature for different AAM mixtures, evaluated on (a) Evaporated
1327 water, (b) Compressive strength, (c) Ultrasonic pulse velocity, (d) MIP porosity and (e) Pore diameter
1328 at half of the main intrusion peak intruded volume (d_{Hm1}). The legend is given in a), 20°C corresponds
1329 to 20°C – 50%RH. Removed water was calculated by comparing the loss of mass with the quantity of
1330 mixing water. Relative strength and velocity were calculated by comparing samples after drying with
1331 the sample of the same age cured in autogenous conditions. The abscissa Endo in ϕ and d_{Hm1} graphs
1332 corresponds to the mean of all autogenous samples. The error bars were calculated with a 95%
1333 confidence interval.

1334

1335 **Table captions**

1336

1337 **Table 1:** Chemical composition in wt% of raw materials obtained with ICP-OES. LOI = loss on ignition.

1338

1339 **Table 2:** Mineralogical composition of the metakaolin, estimated by Rietveld calculation on X-ray
1340 diffractograms following rules described in Trincal et al. [67].

1341

1342 **Table 3:** Mix-designs of the alkali-activated mortars. Units: masses in grams, w/b in %, density in
1343 $\text{g}\cdot\text{cm}^{-3}$.

1344

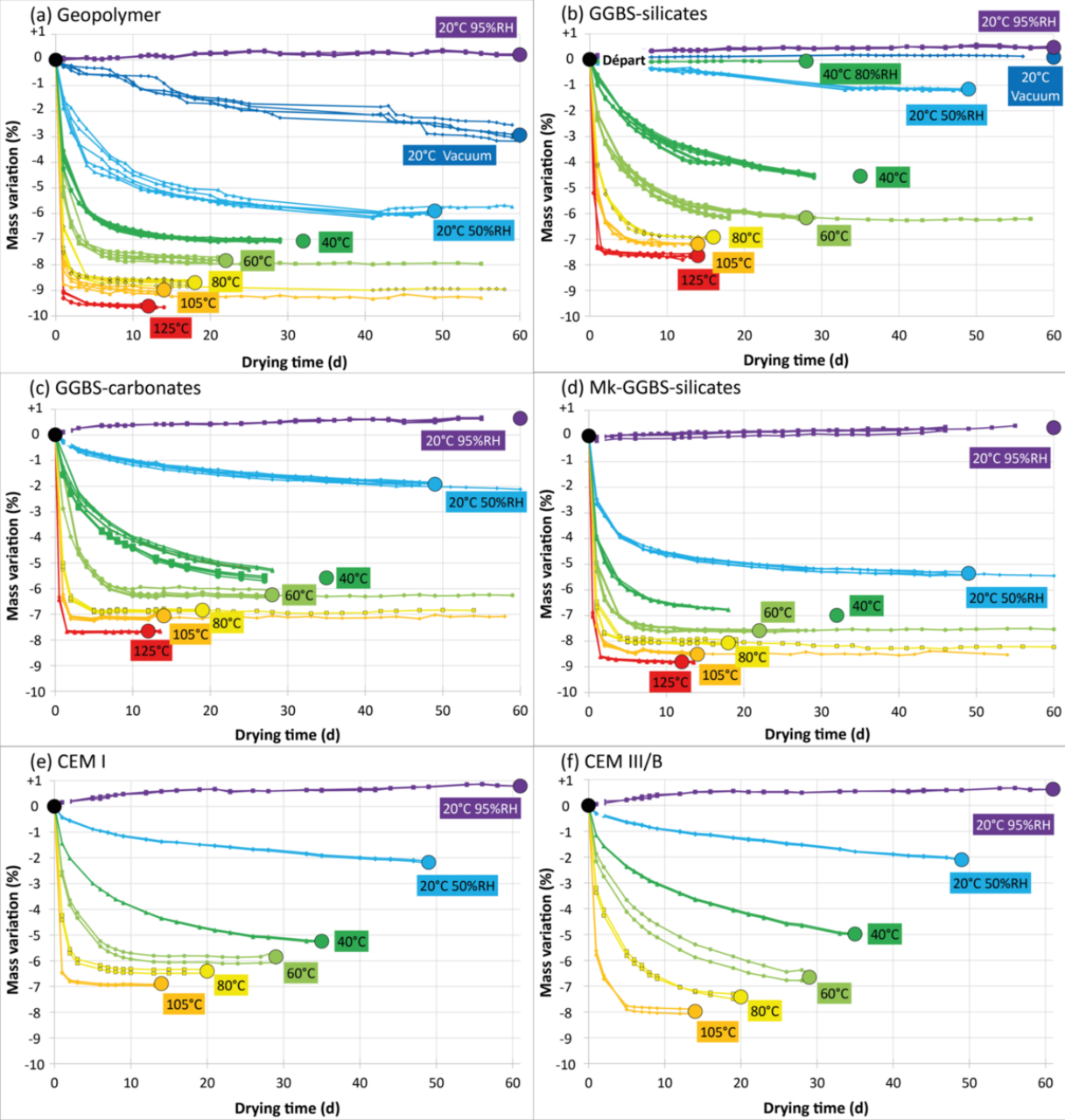
1345 **Table 4:** MIP porosity (φ) in %, degree of pore connectivity (α) in %, and pore diameter (d_{Hm1}) in nm,
1346 corresponding to half of the mercury volume intruded in the main intrusion peak; obtained by MIP
1347 measurements for geopolymer, GGBS-silicate, GGBS-carbonate and Mk-GGBS-silicate after
1348 preconditioning.

1349

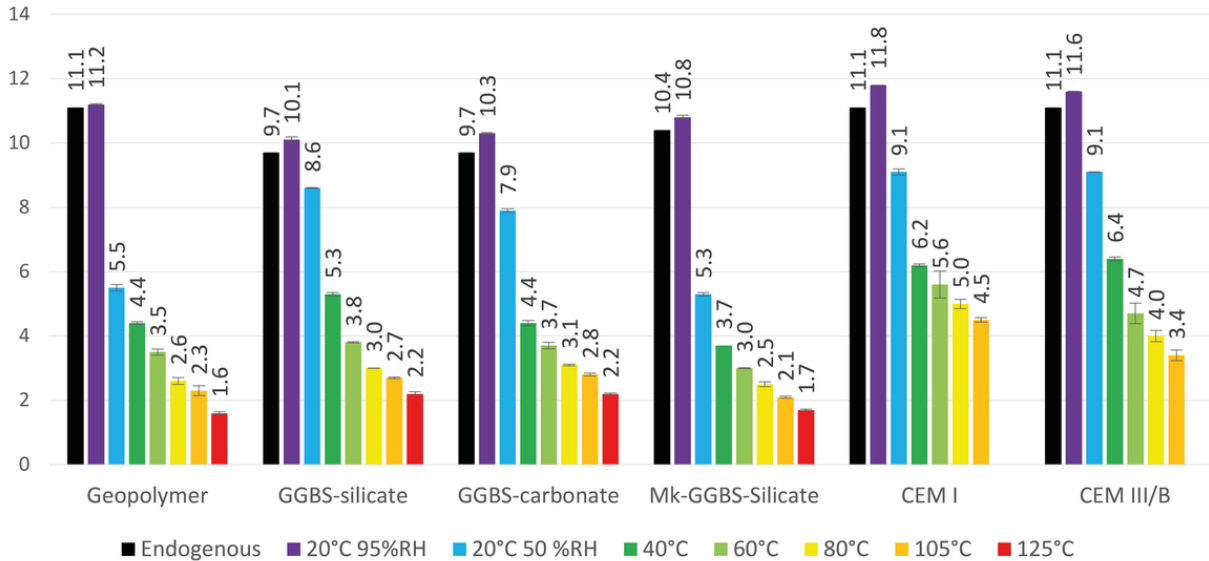
1350 **Table 5:** Drying synthesis.

1351

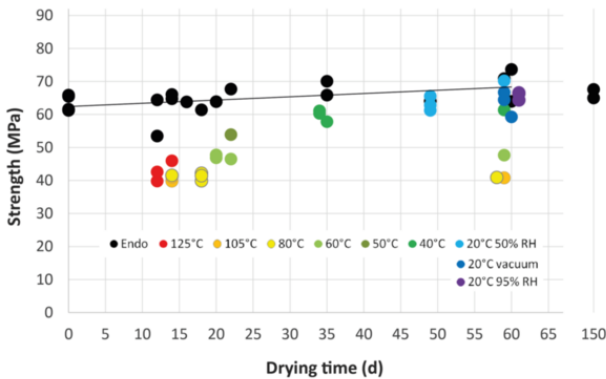
1352



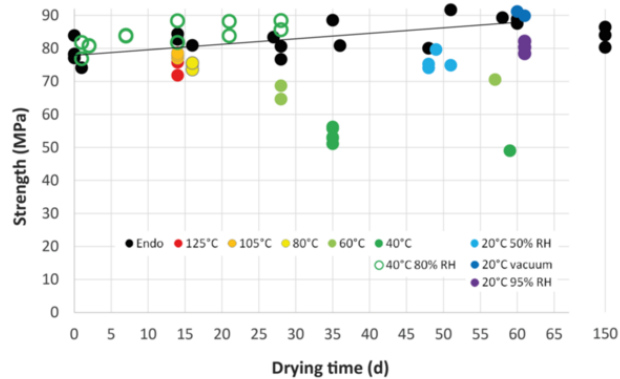
Water content Vw (%)



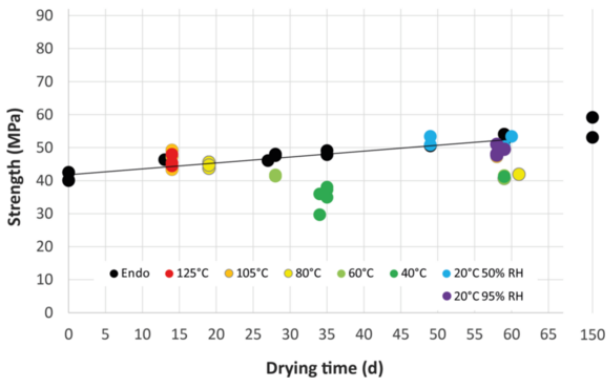
(a) Geopolymer



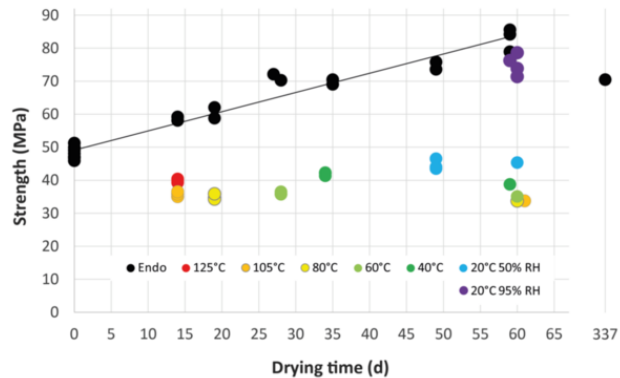
(b) GGBS-silicate



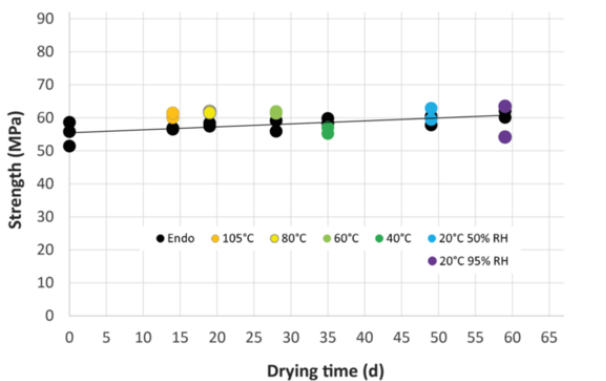
(c) GGBS-carbonate



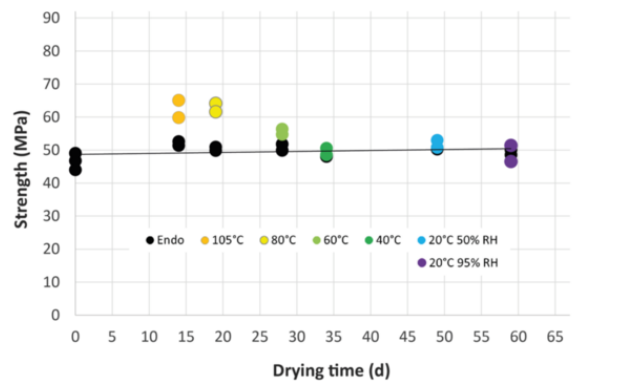
(d) Mk-GGBS-silicate



(e) CEM I

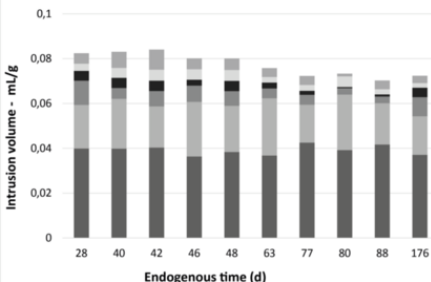


(f) CEM III/B

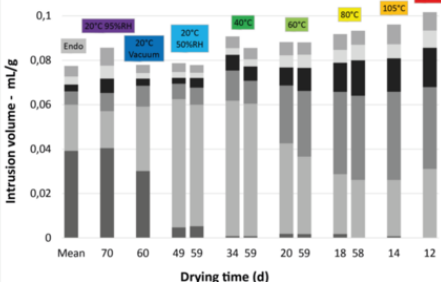


(Top) ■ > 100 000 nm ■ 10 000 - 100 000 nm ■ 1000 - 10000 nm ■ 100 - 1000 nm ■ 10-100 nm ■ <10 nm (Bottom)

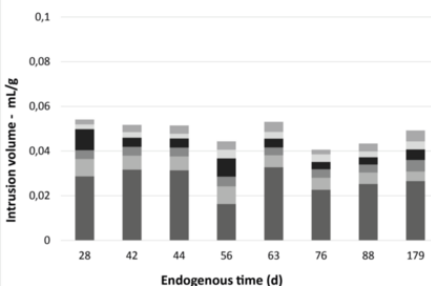
(a) Geopolymer - Endogenous conditions



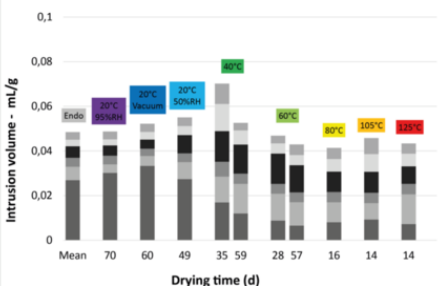
(b) Geopolymer - Drying conditions



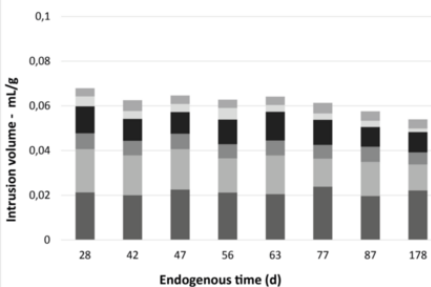
(c) GGBS-silicate - Endogenous conditions



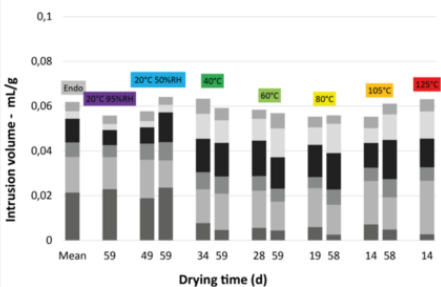
(d) GGBS-silicate - Drying conditions



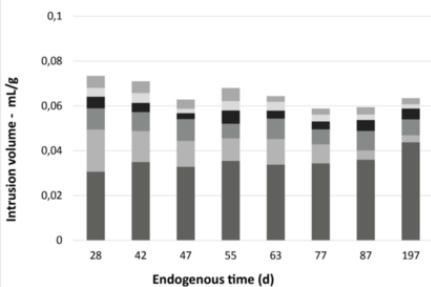
(e) GGBS-carbonate - Endogenous conditions



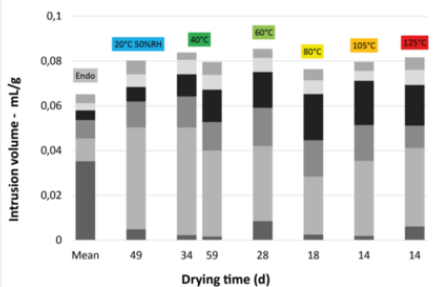
(f) GGBS-carbonate - Drying conditions

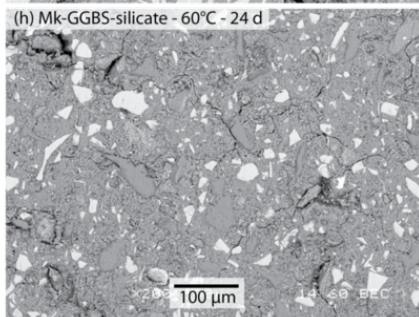
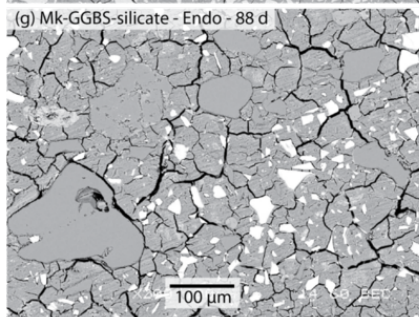
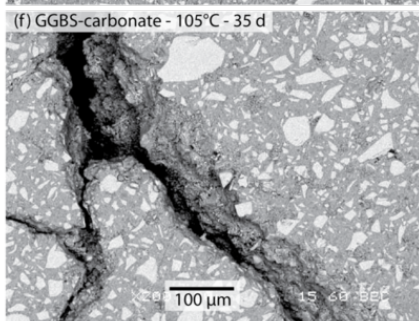
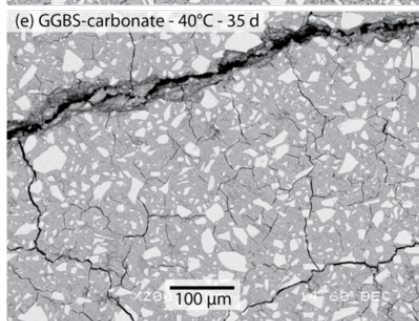
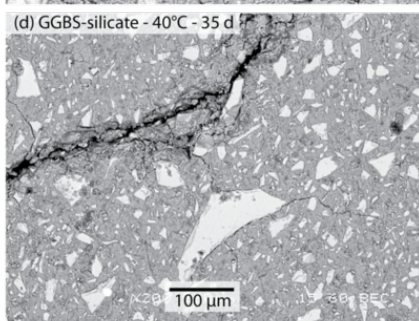
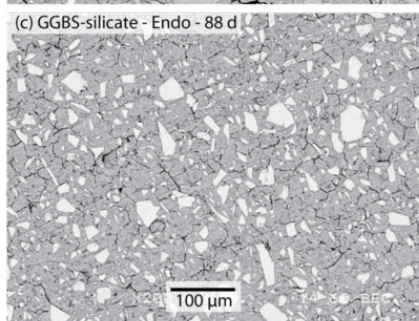
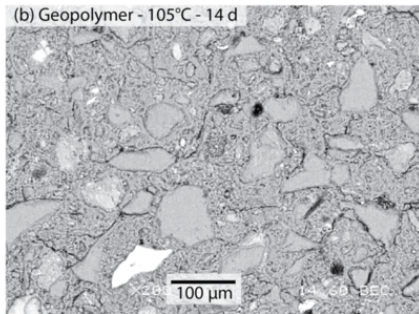
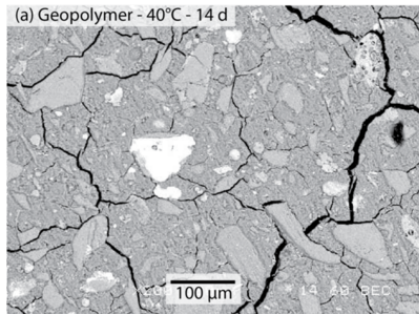


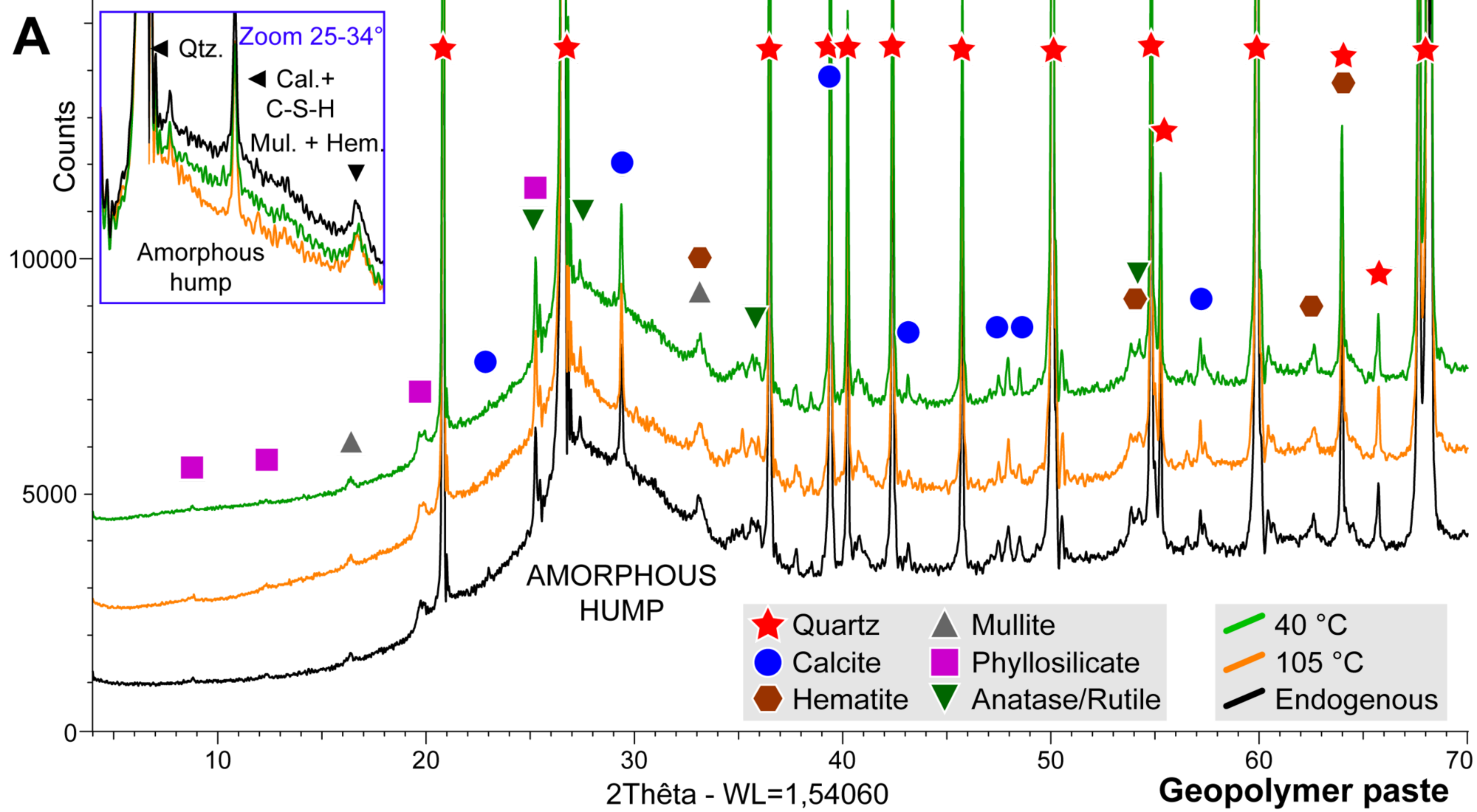
(g) Mk-GGBS-silicate - Endogenous conditions

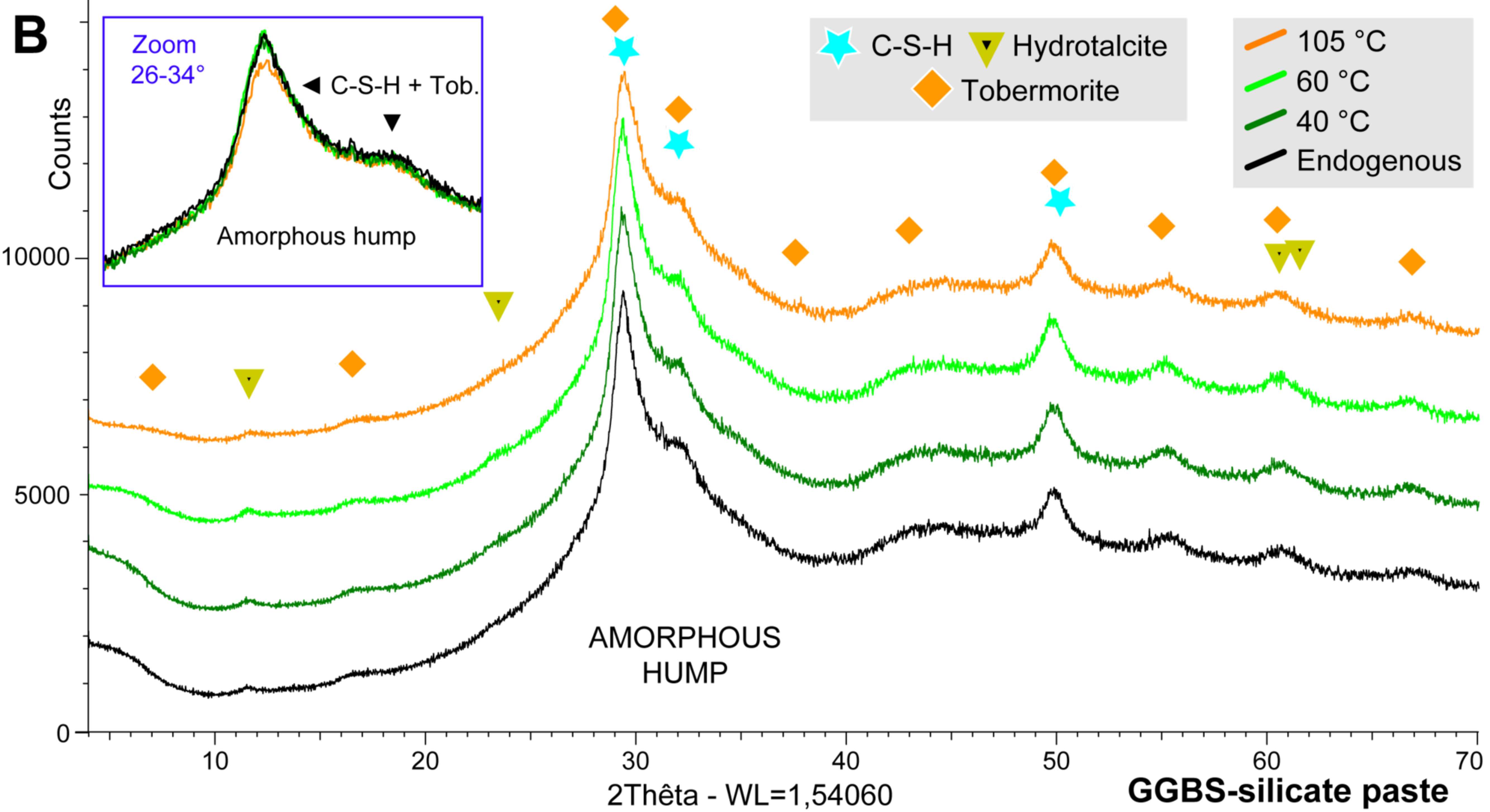


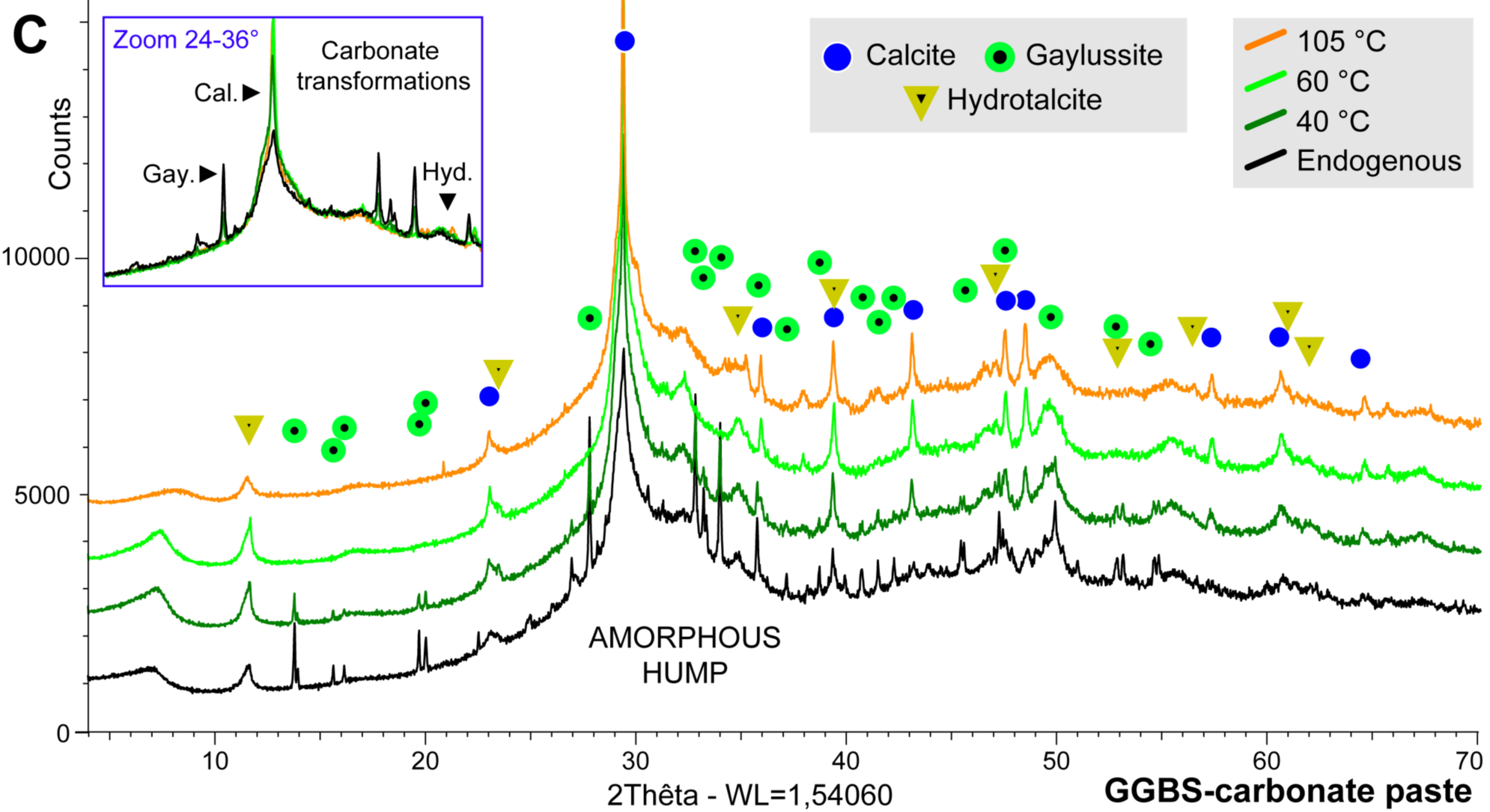
(h) Mk-GGBS-silicate - Drying conditions

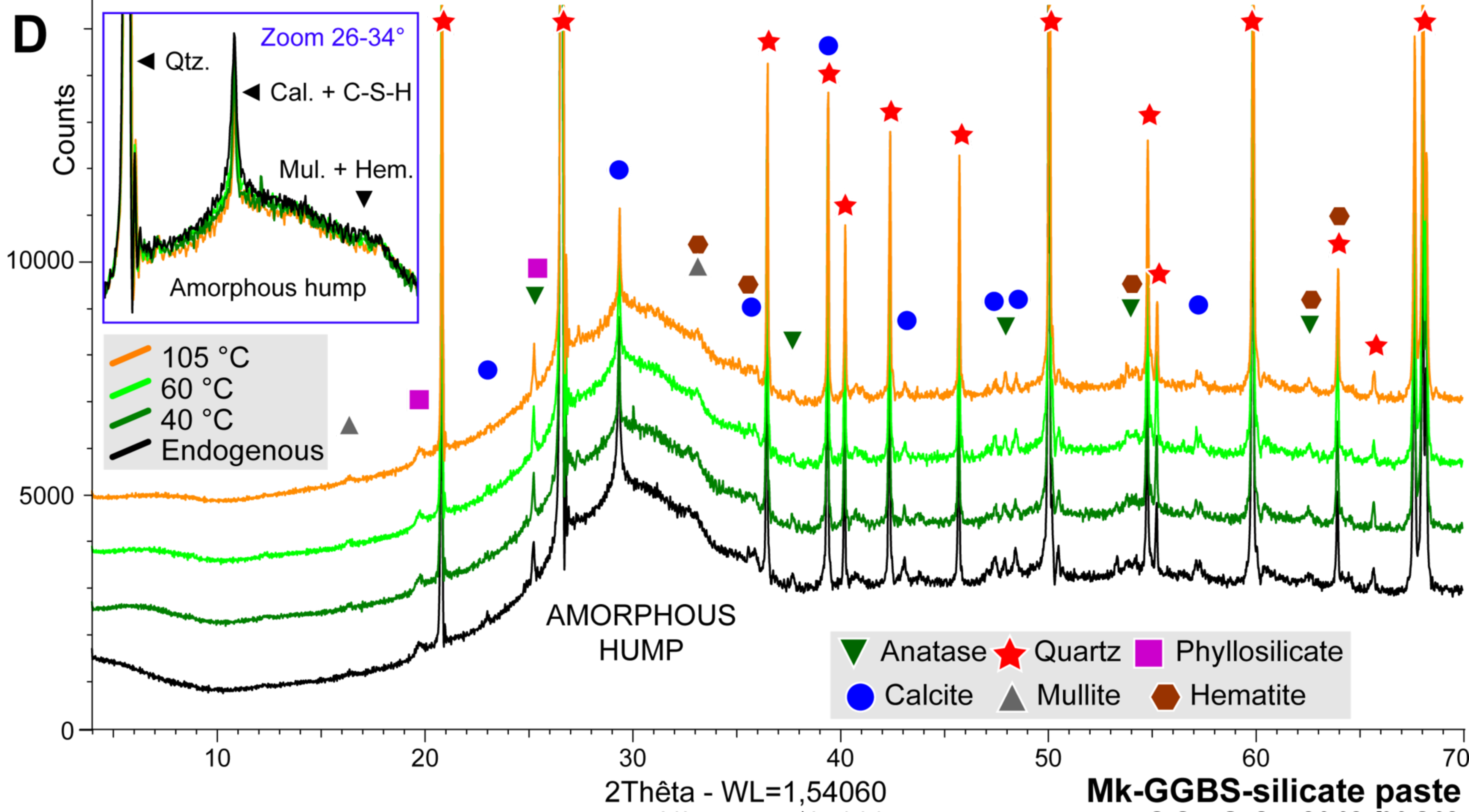


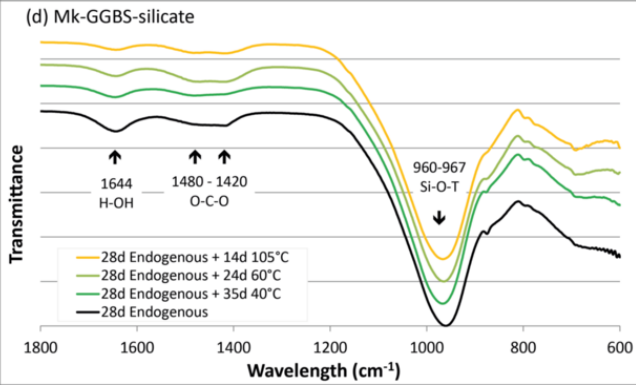
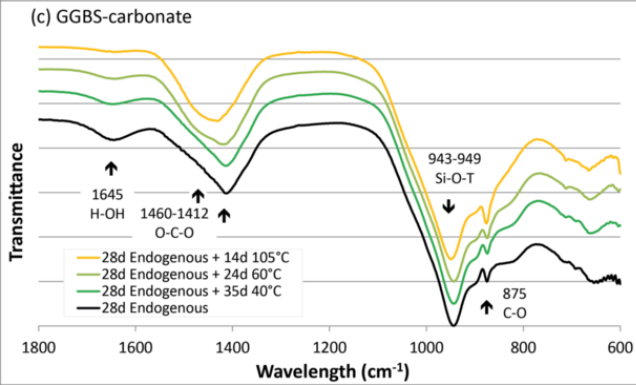
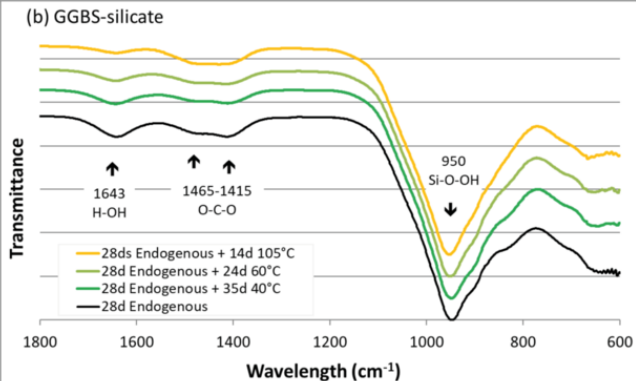
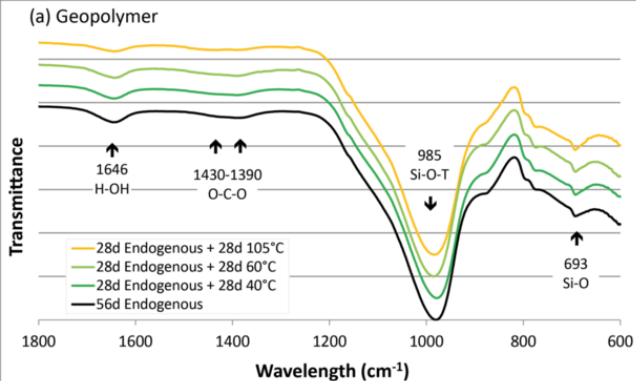


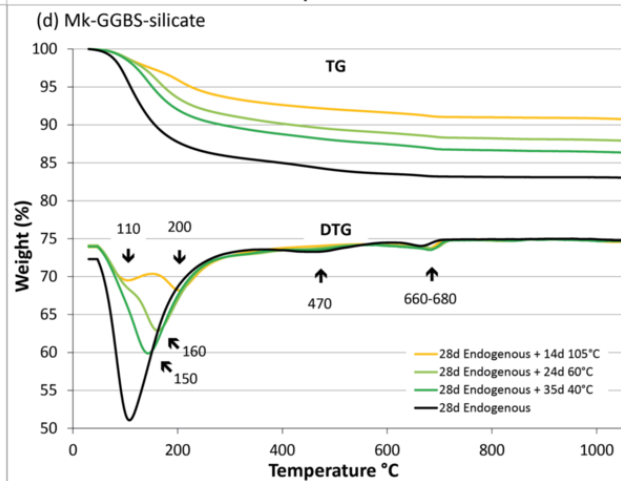
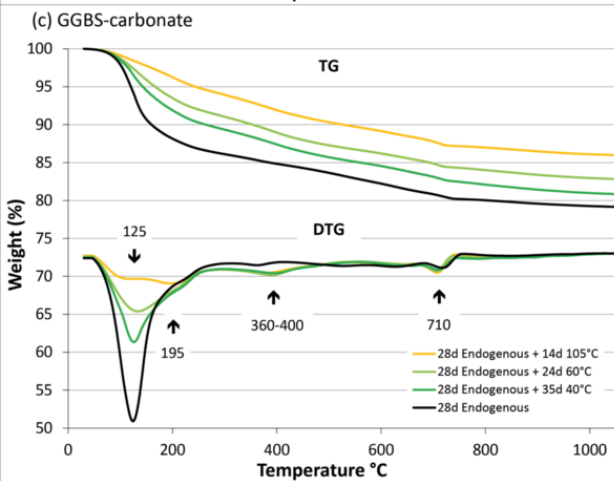
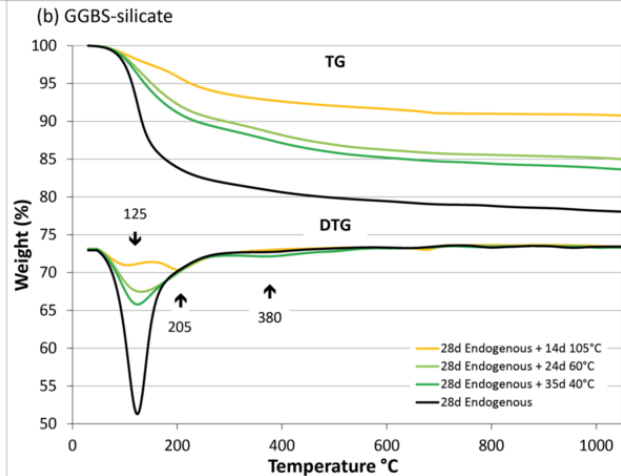
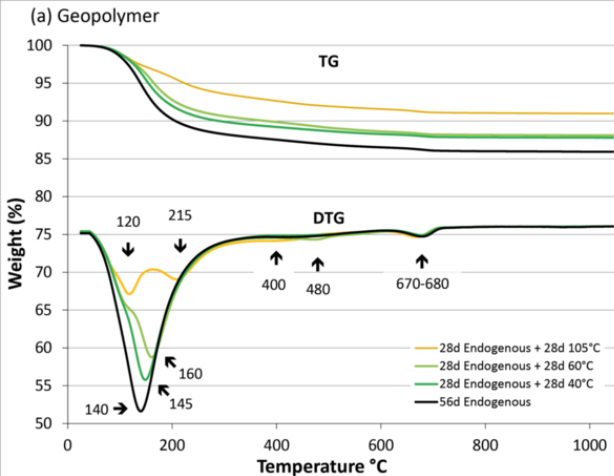




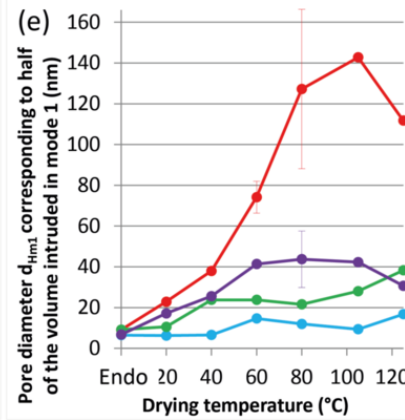
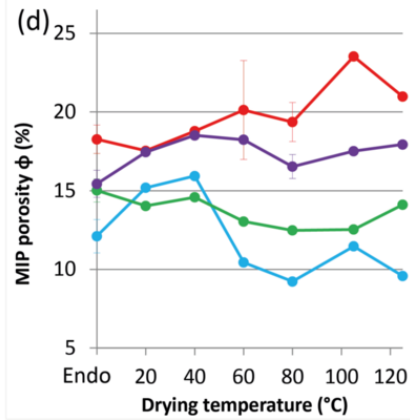
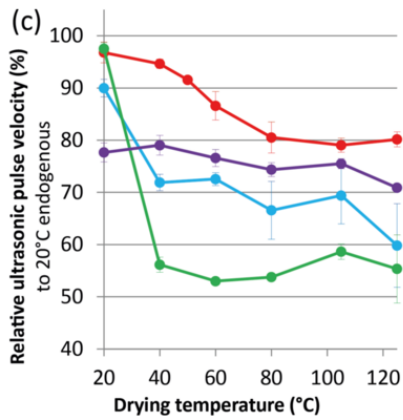
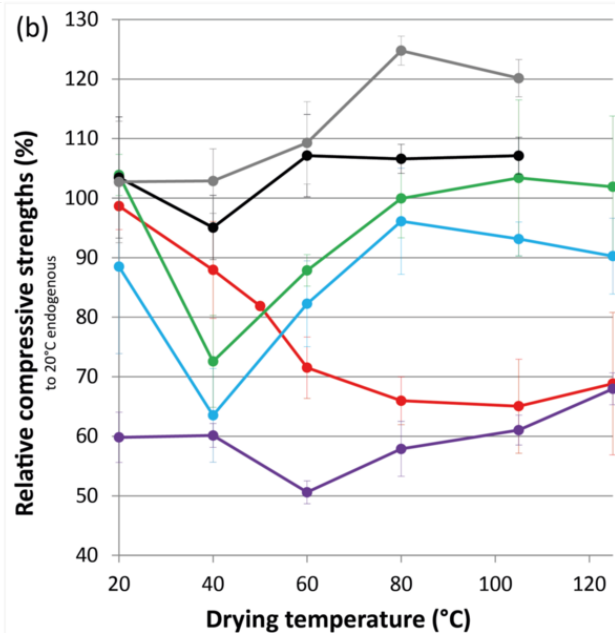
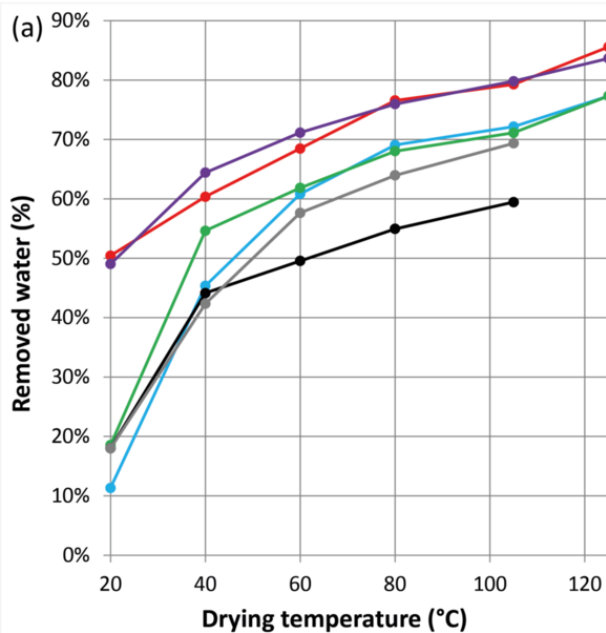








Geopolymer GGBS-silicate GGBS-carbonate MK-GGBS-silicate CEM I CEM III/B



Raw materials	SiO ₂	Al ₂ O ₃	CaO	Fe ₂ O ₃	Na ₂ O	K ₂ O	TiO ₂	MgO	Mn ₂ O ₃	SO ₃	P ₂ O ₅	Cr ₂ O ₃	LOI	Total
CEM I	20.6	4.3	65.5	2.4	0.1	0.2	0.2	0.7	0.1	3.1	0.1	<0.1	2.6	100.0
CEM III/B	30.0	9.5	48.8	2.8	0.5	0.0	0.5	2.7	0.1	2.9	0.2		1.9	100.0
Metakaolin	69.8	22.8	1.2	2.8	0.1	0.3	1.1	0.2	<0.1	<0.1	<0.1	<0.1	1.5	100.0
GGBS	37.5	11.2	42.7	0.4	0.3	0.4	0.7	6.3	0.2	<0.1	<0.1	<0.1	0.0	100.0

Amorphous	47.1 ± 2.5
Quartz	42.3 ± 1.6
Illite	3.5 ± 0.5
Mullite	3.1 ± 0.4
Anatase	1.5 ± 0.1
Calcite	1.0 ± 0.1
Hematite	0.9 ± 0.1
Rutile	0.3 ± 0.1

	Metakaolin	GGBS	CEM I	CEM III/B	Sodium silicate	Sodium carbonate	Water	Sand	W/B	Bulk density
Geopolymer	450.0				354.9		46.2	1350	0.4	2.01
GGBS-silicate		450.0			101.3		141.8	1350	0.4	2.16
GGBS-carbonate		450.0				45.0	198.0	1350	0.4	2.11
Mk-GGBS-silicate	225.0	225.0			228.1		94.0	1350	0.4	2.07
CEM I			450.0				225.0	1350	0.5	-
CEM III/B				450.0			225.0	1350	0.5	-

Condition	Duration	Geopolymer			GGBS-Silicate			GGBS-Carbonate			Mk-GGBS-Silicate		
		ϕ (%)	α (%)	d_{Hm1} (nm)	ϕ (%)	α (%)	d_{Hm1} (nm)	ϕ (%)	α (%)	d_{Hm1} (nm)	ϕ (%)	α (%)	d_{Hm1} (nm)
Autogenous	0d	18.6 ± 1.2	53.2 ± 1.8	9.1 ± 0.6	13.0	71.3	7.1	16 ± 1.1	60.6 ± 1.5	10.2 ± 0.7	17.3	52.8	8.4
	12d	18.1	49.6	9.1									
	14d	18.7	49.8	8.9	14.5	67.7	6.8	15.4 ± 1.5	60 ± 0.4	9.9 ± 2	16.9	52.4	7.2
	16d				14.5	71.1	6.6						
	18±1d	20.7	50.8	9.7				15.7	58.1	9.4	14.8	53.8	7.5
	20d	20.7	50.0	9.4									
	28±1d				11.3	62.5	6.8	15.1 ± 3.2	61.9 ± 0.3	8.9 ± 2.8	16.0	59.4	6.8
	35d	17.6	53.7	9.5	13.8 ± 2.3	68.6 ± 5	6.4 ± 0.3	15.2	62.4	9.6	14.9	53.3	6.8
	48±1d	16.7	48.3	8.6	10.1	66.2	6.6	14.4	59.7	7.6	14.3	57.6	6.8
	52d	18.8	56.0	9									
	60±1d	16.5	48.5	8.7	10.6 ± 1	62.2 ± 2	6.5 ± 0.3	13.9	60.6	9.1	13.8	54.3	5.7
	158±11d	16.1	52.1	9	12.0	63.4	5.9	13.0	60.3	7.7	15.5	47.5	5.0
125°C	13±1d	21.0	44.5	111.8	9.6	58.0	16.8	14.1	66.1	38.3	17.9	46.5	30.7
105°C	14d	23.5	47.0	142.8	11.5	65.4	7.5	12.5	59.4	28.1	17.5	44.6	42.3
	58d							13.7	68.8	29.8			
80°C	18±2d	19.4 ± 1.2	46.7 ± 2	127.3 ± 39.1	9.2	59.2	12.0	12.5	63.0	21.6	16.5 ± 0.8	55.5 ± 2.5	43.8 ± 13.8
	58±1d	19.8 ± 2.1	46.7 ± 1.2	143.3 ± 0.1				12.5	74.0	28.4			
60°C	20d	20.1 ± 3.1	45 ± 1.6	74.2 ± 7.8									
	28d				10.4	55.1	14.7	13.0	64.2	23.8	18.2	46.5	41.4
	59d	18.7	44.7	87.9	10.0	60.3	18.4	12.5	72.2	24.2			
40°C	34±1d	18.8	48.7	38	15.9	51.0	6.6	14.6	57.5	23.8	18.5	50.5	25.6
	59d	17.5	46.6	37.5	12.0	51.4	13.5	14.1	68.0	32.3	17.0	51.5	32.4
20°C-50%RH	49d	17.5	47.8	22.9	15.2	61.0	6.3	14.0	59.8	10.6	17.5	51.7	17.2
	59d	17.3 ± 0.2	49.3 ± 1.1	22.8 ± 3				14.4	58.5	6.8			
Vacuum	60d	17.0	49.5	12.1	12.7 ± 1	59.9 ± 4	5.9 ± 0.2						
20°C 95%RH	59d							13.9	59.4	8.0			
	70d	19.0	53.3	8.7	11.6	73.4	5.9						

Drying condition	Geopolymer	GGBS-silicate	GGBS-carbonate	Mk-GGBS-silicate
20°C 50%RH	Slow (2-4 weeks), efficient (50-60%) drying; no strength damage; porosity little changed; no mineralogical transformation	Very slow (>2 months), inefficient (<25%) drying; no strength damage; porosity not changed; no mineralogical transformation	Very slow (>2 months), inefficient (<30%) drying; no strength damage; porosity not changed; no mineralogical transformation	Slow (2-3 weeks), efficient (50-67%) drying; strength damage; porosity changed; mineralogical transformations
40°C (low RH)		Slow (2-4 weeks), efficient (50-67%) drying; strength damage; porosity little changed; no mineralogical transformation	Slow (1-4 weeks), efficient (60-67%) drying; strength damage; porosity little changed; mineralogical transformations	
60°C	Fast (<1 week), efficient (65-85%) drying; strength damage; pore size changed significantly; no mineralogical transformation	Fast (<1 week), efficient (70-80%) drying; no strength damage; pore size little changed; no mineralogical transformation	Fast (<1 week), efficient (70-80%) drying; no strength damage; pore size little changed; mineralogical transformations	Fast (<1 week), efficient (65-85%) drying; strength damage; pore size changed significantly; mineralogical transformations
80°C				
105°C				
125°C				